NUMERICAL INVESTIGATION OF CONVECTIVE-DIFFUSIVE TRANSPORT USING THE SMOOTHED PARTICLE HYDRODYNAMICS TECHNIQUE

by

Mustafa Engin Danış

B.S, in Mechanical Engineering, Boğaziçi University, 2010

B.S, in Physics, Boğaziçi University, 2010

Submitted to the Institute for Graduate Studies in
Science and Engineering in partial fulfillment of
the requirements for the degree of
Master of Science

Graduate Program in Mechanical Engineering

Boğaziçi University

2012

NUMERICAL INVESTIGATION OF CONVECTIVE-DIFFUSIVE TRANSPORT USING THE SMOOTHED PARTICLE HYDRODYNAMICS TECHNIQUE

APPROVED BY:

Assoc. Prof. Ali Ecder .....
(Thesis Supervisor)

Assist. Prof. Mehmet Orhan .....
(Thesis Co-supervisor)

Prof. Günay Anlaş .....

Assoc. Prof. Hasan Bedir .....

Assist. Prof. Fatih Ecevit .....

DATE OF APPROVAL:

ACKNOWLEDGEMENTS

First of all, I would like to express my gratitude to my advisor Assoc. Prof. Ali Ecder for his continuous support and guidance. Under his supervision, I found the chance to deepen my knowledge. I'm also thankful to Assist. Prof. Mehmet Orhan for suggesting the subject of this thesis and his valuable comments. Moreover, I appreciate Prof. Günay Anlaş, Assoc. Prof. Hasan Bedir and Assist. Prof. Fatih Ecevit for their guidance and opinions on my thesis.

I'm also grateful to Prof. Alpar Sevgen not only for teaching me Physics but also for expanding my vision of life. With his great knowledge and experience, he always tried to push me forward. I deeply appreciate this.

I would like to thank my friends for their support and understanding, especially, Aidin Sheikhi whose companionship will never be forgotten.

Lastly, my deepest thanks and gratitude go to my father Kenan Danış, my mother Yıldız Danış, my sister Elif Yılmaz and my beloved wife Nergis Danış. Without their constant support, encouragement and love, this thesis would never come to an end. They always believed in my dreams and never doubted me. I greatly appreciate this.

ABSTRACT

NUMERICAL INVESTIGATION OF CONVECTIVE-DIFFUSIVE TRANSPORT USING THE SMOOTHED PARTICLE HYDRODYNAMICS TECHNIQUE

In this thesis, Incompressible Smoothed Particle Hydrodynamics (ISPH) technique is implemented to analyze various convective-diffusive transport problems numerically. First of all, a brief summary of applications and developments in SPH is given. Then, SPH methodology is presented. A detailed discussion on frequently used high order SPH approximation schemes is made and an expansion of existing projection methods developed for isothermal flow to non-isothermal and double-diffusive flows is introduced. The code developed during this thesis study is validated for isothermal problems such as lid-driven cavity and vortex spin-down. Furthermore, in order to test the upper limit of accuracy of SPH computations, a grid-based ISPH approach is proposed. Grid-based ISPH is applied to natural convection in a square cavity problem and the results are compared to the data available in the literature. Similar to grid-based ISPH code, meshless ISPH code is used to solve natural convection problems. Rayleigh-Bénard convection is studied and multiple states of the solutions are obtained. Moreover, natural convection is investigated at the onset of instability in which multicellular and oscillatory flow patterns are observed. Apart from natural convection, ISPH code also introduced to double-diffusive transport problems. In terms of double-diffusion, ISPH performance in aiding and opposing flows are provided. Furthermore, ISPH code is also implemented to two-phase flows. In the context of two-phase flows, topological changes of the interfaces and Rayleigh-Taylor instability problems are simulated. ISPH results for two-phase flow are compared to results obtained by Level Set Method.

ÖZET

TAŞINIMSAL-YAYINIMSAL İLETİMİN DÜZLEŞTİRİLMİŞ PARÇACIK HİDRODİNAMİĞİ YÖNTEMİ İLE SAYISAL OLARAK ARAŞTIRILMASI

Bu tezde, Sıkıştırılamayan Düzleştirilmiş Parçacık Hidrodinamiği (ISPH) tekniği, birçok taşınımsal-yayınımsal iletim probleminin sayısal analizi için uygulanmıştır. İlk olarak, SPH'deki uygulamaların ve gelişmelerin kısa bir özeti verilmiştir. Sonrasında, SPH metodolojisi sunulmuştur. Sıkça kullanılan yüksek mertebeden SPH yaklaştırım yöntemleri üzerine detaylı bir tartışma yapılmış ve izotermal akışlar için geliştirilmiş olan izdüşüm yöntemlerinin ısıl ve çifte yayınımlı akışlar için genişletilmesi tanıtılmıştır. Tez çalışması esnasında geliştirilen kod, kapak tahrikli kare oyuk akışı ve girdap sönümü gibi izotermal akışlar için doğrulatılmıştır. Ayrıca, SPH hesaplamalarının hassasiyetinin üst limitini test etmek için ağ temelli ISPH yaklaşımı önerilmiştir. Ağ temelli ISPH, kare bir oyuktaki doğal taşınım problemine uygulanmış ve sonuçlar literatürde varolan sonuçlar ile kıyaslanmıştır. Ağ temelli ISPH gibi, ağsız ISPH kodu da doğal taşınım problemlerini çözmek için kullanılmıştır. Rayleigh-Bénard taşınımı çalışılmış ve çoklu çözüm durumları elde edilmiştir. Ek olarak, kararsızlık başlangıcındaki çoklu hücresel ve salınımlı akış yapıları gözlemlenen doğal taşınım problemleri araştırılmıştır. Doğal taşınım haricinde, ISPH kodu çifte yayınınım problemlerine de uygulanmıştır. Çifte yayınım bakımından, ISPH'nin performansı "Destekleyen" ve "Karşı" akışlar için gösterilmiştir. Bunlara ek olarak, ISPH kodu iki fazlı akışlara da uygulanmıştır. İki fazlı akışlar kapsamında, arayüzeylerin topolojik değişimleri ve Rayleigh-Taylor kararsızlık problemi simule edilmiştir. İki fazlı akışlar için elde edilen ISPH sonuçları Düzey Kümesi Yöntemi ile elde edilen sonuçlar ile kıyaslanmıştır.

TABLE OF CONTENTS

LIST OF FIGURES

LIST OF TABLES

LIST OF SYMBOLS

AR	Aspect Ratio
C	Concentration
C_L	Dimensionless Low Concentration
C_H	Dimensionless High Concentration
C^*	Dimensionless Concentration
C^0	Reference Concentration
D	Coefficient of Solutal Diffusivity
g	Acceleration of Gravity
$\vec{f}$	Body Forces
h	Smoothing Length
$\mathbf{L}$	Inverse of Kernel Gradient Correction Matrix
L	Characteristic Length
Le	Lewis Number
m	Mass
Ma	Mach Number
Nu	Mean Nusselt Number at the Wall
Nu_{max}	Maximum Nusselt Number at the Hot Wall
Nu_{min}	Minimum Nusselt Number at the Hot Wall
P	Pressure
$\tilde{P}$	Pressure including Hydrostatic Effects
P^*	Dimensionless Pressure
P_0	Reference Pressure
Pr	Prandtl Number
Ra	Rayleigh Number
Ra_T	Thermal Rayleigh Number
Ra_S	Solutal Rayleigh Number
Re	Reynolds Number
t	Time

t^*	Dimensionless Time
T	Temperature
T_C	Dimensionless Cold Temperature
T_H	Dimensionless Hot Temperature
T^*	Dimensionless Temperature
T^0*	Reference Temperature
$\vec{u}$	Velocity Vector
u	x-component of Velocity Vector
$\vec{u}^*$	Dimensionless Velocity Vector
u^*	x-component of Dimensionless Velocity Vector
U_0	Reference Velocity
v	y-component of Velocity Vector
v^*	y-component of Dimensionless Velocity Vector
$W(\vec{r}-\vec{r}')$	Smoothing Kernel Function
α	Coefficient of Thermal Diffusivity
β_T	Coefficient of Thermal Expansion
β_S	Coefficient of Solutal Expansion
δ	Dirac Delta Function
ε	Interface Thickness
μ	Dynamic Viscosity
ν	Kinematic Viscosity
ρ	Density
ρ_0	Reference Density
ρ^*	Dimensionless Density
ϕ	Level Set Function

LIST OF ACRONYMS/ABBREVIATIONS

2D	Two Dimensional
BiCGSTAB	Bi-conjugate Gradient Stabilized
CFD	Computational Fluid Dynamics
CFL	Courant − Friedrichs − Lewy
CG	Conjugate Gradient
LS	Level Set
SPH	Smoothed Particle Hydrodynamics
ISPH	Incompressible Smoothed Particle Hydrodynamics
ISPH-DF	Divergence Free Incompressible Smoothed Particle Hydrodynamics
ISPH-DFS	Divergence Free Incompressible Smoothed Particle Hydrodynamics with Particle Shifting
ISPH-DFDI	Divergence Free and Density Invariant Incompressible Smoothed Particle Hydrodynamics
ISPH-DI	Density Invariant Incompressible Smoothed Particle Hydrodynamics
LES	Large Eddy Simulation
MAC	Marker and Cell
MD	Molecular Dynamics
PIC	Particle in Cell
PSPH	Projection Smoothed Particle Hydrodynamics
VOF	Volume of Fluid
WCSPH	Weakly Compressible Smoothed Particle Hydrodynamics

1. INTRODUCTION

Smoothed Particle Hydrodynamics (SPH) is originally invented by Lucy [1] and, Gingold and Monaghan [2] as a truly meshless Lagrangian method in order to simulate astrophysical problems. Although it was invented to solve astrophysical problems, SPH is now has a wide range of applications in fluid mechanics, solid mechanics, high velocity impact problems, film and computer games industry.

In SPH, a continuum is modeled by a finite set of particles that can freely move in computational domain. These particles are not physical particles. Instead, SPH particles are hypothetical particles and they may be thought as moving versions of fixed Eulerian grid nodes but obeying Lagrangian form of governing equations. Since particles can change their position in a certain time period, they do not have geometrically fixed relations with each other. For instance, an interaction between any two particles may change at a later time step and even may not exist anymore. Thus, fixed discretization schemes in grid-based methods, e.g. finite difference, cannot be used in meshless methods. In order to model and discretize a continuum, the particle interactions are defined by smoothing kernels (smoothing functions or weighting functions) in SPH [3]. In a neighborhood of a specified particle, the smoothing kernels are used to calculate how much effect neighboring particles have on this specified particle. Thus, in a typical SPH time step, neighbor list for each particle must be constructed and smoothing kernels and their derivatives must be calculated immediately after particles are moved. All mathematical operators in governing equations (e.g. derivative, gradient, divergence and laplacian) are discretized and calculated according to neighbor list, smoothing kernel and derivatives of smoothing kernel. For a field variable (e.g. position, velocity, temperature, density etc.) inserting the obtained values of mathematical operators into governing equations, material time rate of change is calculated and particles are moved. At the new position, new values for field variables are obtained by implementing a proper numerical integration scheme. This process is repeated until steady state is reached.

First incompressible flow simulation using SPH was performed by Monaghan [4] in which free surface flows such as elliptical drop, bursting dam, bore and wavemaker problems were studied. One of the most interesting features of this work is that incompressibility was approximated by weakly compressible approach. This is based on the observation that density variation is proportional to square of Mach number, Ma^2. However, speed of sound in an incompressible fluid is very large and Mach number is very small. Therefore, incompressible fluid is approximated with an artificial fluid in which speed of sound is decreased and Mach number is increased. It is worth to note that Mach number is still small enough to approximate an incompressible fluid. In SPH literature, Mach number is usually chosen between 10^{-1} and 10^{-2}. Thus, density variation changes from 10^{-2} to 10^{-4}, which means that flow is nearly incompressible. Another interesting feature of this work is that pressure was treated as a function of density and calculated from an equation of state. This approach is known as "*Weakly Compressible SPH (WCSPH)*" and today, it is one of the most popular SPH approaches for incompressible flow simulations.

Another incompressible approach was also presented by Morris *et al.* [5] in which low Reynolds number problems such as Couette flow, Poiseuille flow and flow past a cylinder were simulated. As opposed to the equation of state used by Monaghan [4], Morris *et al.* [5] used a different equation of state. Furthermore, in order to model solid boundaries, Morris *et al.* [5] introduced mirror particle method first time in SPH simulations. This is another difference from work of Monaghan [4] where a repulsive force is used in order to model solid boundaries, which is very similar to Lennard-Jones force in Molecular Dynamics (MD) simulations.

However, classical Weakly Compressible SPH approach has some limitations and weaknesses. For instance, it is not be able to simulate moderate or high Reynolds number flows accurately. Therefore, instead of the classical WCSPH approach, advanced approaches are implemented to WCSPH. Using proper turbulence models, WCSPH is able to simulate high Reynolds number flows (e.g. Gomez *et al.*, [6] Shao *et al.* [7]). Moreover, increasing speed of sound decreases time increment limit due to CFL condition. Therefore, computational time and effort spent to reach steady state is increased.

In addition to these, pressure field is very sensitive to density fluctuations since pressure is calculated as function of density using an equation of state in Weakly Compressible SPH. Therefore, fluctuations in density field result in oscillations in pressure field. Therefore, several approaches are introduced in order to reduce density fluctuations and resulting oscillations in pressure field.

One of these approaches is called "*Incompressible SPH (ISPH)*". In ISPH method, incompressibility is directly enforced and an intermediate velocity field is obtained without considering gradient of pressure. The intermediate velocity field is, then, projected onto a divergence-free velocity space which results in a pressure Poisson equation. After solving pressure Poisson equation, intermediate velocity field is corrected to obtain a new velocity field which is divergence-free. This method is based on Helmholtz-Hodge Decomposition and it was first introduced to SPH context by Cummins and Rudman [8]. In their study, this projection approach was termed PSPH but nowadays, it is usually called "*Divergence Free Incompressible SPH* (ISPH-DF)".

Similar to SPH projection method presented by Cummins and Rudman [8], Shao and Lo [9] suggested another SPH projection approach that enforces incompressibility by using density invariance. In their method, an intermediate velocity field is calculated without considering gradient of pressure as in Cummins and Rudman [8]. At this stage instead of projecting the intermediate velocity field onto a divergence free velocity field, density variation is projected onto a Divergence-Free velocity field. By this way, accumulation of density errors in divergence-free ISPH is not observed. This approach is called "*Density Invariant Incompressible SPH* (ISPH-DI)". They used their approach for simulations of near-shore solitary wave mechanics with a Large Eddy Simulation (LES).

Another projection based incompressible SPH method was introduced by Pozorski and Wawrenczuk [10]. A procedure similar to that was presented by Cummins and Rudman [8] was followed. At the end of each time step, an additional pressure Poisson equation is solved in order to obtain a constant density field and particle positions are updated due to resulting pressure gradient. They tested their algorithm for one

dimensional viscous damping, Couette and Poiseuille flows, lid-driven cavity flow and Rayleigh-Taylor instability problems.

Furthermore, Colin *et al.* [11] proposed a pure SPH solution of Helmholtz-Decomposition in order to obtain a null divergence field. Moreover, a new version of Laplacian operator was introduced. In addition to these, different SPH gradient operators were compared. They concluded that difference gradient approximation formula gives better results and it is more compatible with the new Laplacian operator.

Moreover, Hu and Adams [12] suggested an approach similar to Pozorski and Wawrenczuk [10] by combining ISPH-DF and ISPH-DI in order to simulate multiphase incompressible flows. This method is known as "*Divergence Free and Density Invariant Incompressible SPH* (ISPH-DFDI)". In this approach, first of all, density invariant approach is utilized as internal iterations until density variation is lower than a desired tolerance. In other words, density projected pressure Poisson equation is solved and particle positions are updated repeatedly until uniform particle distribution is obtained. After the internal iterations are completed, divergence free approach is utilized in order to obtain a divergence free velocity field. In the best case, two pressure Poisson equation is solved in each time step and if a uniform particle distribution is not obtained at the first internal iteration, number of internal pressure Poisson equations to be solved is increased. Although this increases computational cost, this approach results in uniform particle distribution and thus, increased accuracy.

In addition to these, Xu *et al.* [13] introduced a particle shifting method which prevents anisotropic particle distribution resulting in ISPH methods together with an extensive comparison of ISPH-DF, ISPH-DI and ISPH-DFDI. According to Xu *et al.* [13], hydrodynamic variables are corrected using a Taylor series expansion and anisotropic in particle distributions are avoided. Although the particle shifting method is not a strictly conservative method, it increases accuracy of simulations. This approach is called *Divergence Free Incompressible SPH with shifting particle position* (ISPH-DFS). In study of Xu *et al.* [13], accuracy tests were performed for Taylor-Green vortices and Vortex Spin-down problems. Moreover, ISPH-DFS method was validated with

benchmark problems lid-driven cavity and two dimensional laminar flow past a circular cylinder. Free surface flows (e.g. impulsive paddle and two dimensional dam break) were investigated using ISPH-DFS method.

Szewc *et al.* [14] investigated the incompressibility constraint in SPH. They analyzed WCSPH, grid projected ISPH and particle projected ISPH for the same kind of boundary conditions for a direct comparison of these approaches. They pointed out accumulation of density error in ISPH simulation. In order to prevent accumulation of density errors, they made use of the incompressible SPH algorithm proposed by Pozorski and Wawrenczuk [10]. However, they suggested to include second pressure Poisson equation if density variation exceeds a certain threshold value. Therefore, they reduced computational cost as well as density variation.

A different approach for solving pressure Poisson equation was presented by Hosseini *et al.* [15]. They proposed a three step explicit algorithm for simulation of non-Newtonian fluid flow in which pressure Poisson equation was solved explicitly. In their work, Hosseini *et al.* [15] only included body force terms in the first step. In the second step, viscous terms were included and density variation was projected onto a divergence-free velocity field. After solving pressure Poisson equation explicitly, velocity field and particle positions were corrected in the third step.

In general, projection based Incompressible SPH approaches make use of an iterative method in order to solve pressure Poisson equation implicitly. In SPH literature, the most common solvers are Conjugate Gradient(CG) and Bi-Conjugate Gradient Stabilized(BiCGSTAB) methods. Especially, BiCGSTAB is preferred since it smooths out the residual and enhance the convergence according to van der Vorst [16].

Apart from projection based ISPH methodologies, Ellero *et al.* [17] presented a different ISPH approach. They used Lagrange multipliers in order to enforce incompressibility and set constant volume of the fluid particles as their kinematic constraint. Then, they solved the constraint equation using the SHAKE methodology in order to obtain Lagrange multipliers which are the non-thermodynamics pressure values result-

ing from kinematic restrictions.

Usage of SPH in incompressible flow simulations is not limited to isothermal case. Chaniotis *et al.* [18] proposed a remeshing algorithm using weakly compressible approach and performed a comprehensive study for nonisothermal flows. Remeshing procedure was tested for some benchmark problems of flow and energy transport such as one dimensional shock-tube problem, two dimensional Taylor-Green flow, two dimensional double shear layer, lid-driven flow in a square cavity, natural convection in a differentially heated cavity and mixed convection in a driven cavity. Results showed that remeshing improved the accuracy of simulations since uniform particle spacing was conserved in each time step. Moreover, Chaniotis *et al.* [18] used remeshing procedure in the study of effect of jet pulsation on heat transfer and flow characteristics of single and double jet impingement on a heated surface, simulation of laminar chemically reacting and interfacial flows.

Another simulation of flow and energy transport using SPH was performed by Szewc *et al.* [19]. Natural convection in a square cavity problem with a Boussinesq and a non-Boussinesq formulation was studied. They performed simulations at $Ra = 10^3$, $Ra = 10^4$ and $Ra = 10^5$ with $Pr = 0.71$. They investigated the effect of Gay-Lussac number on velocity field and Nusselt number for non-Boussinesq formulation. They reported that their results were in good-agreement with other numerical experiments. Since they used weakly compressible approach, velocity and temperature fields showed oscillations.

Although SPH achieves a great success in simulating fluid flow accurately, there are still certain limitations due to the meshfree character of the method. One of these limitations is the tensile instability problem, which results in clustering of particles [20]. Since a uniform distribution of particles is necessary for incompressible flow simulations, the tensile instability problem was tried to be overcome by introducing artificial pressure (e.g. Monaghan [20]), projection methods (e.g. Cummins and Rudman [8], Shao and Lo [9], Hu and Adams [12]) and particle shifting techniques (e.g. Xu *et al.* [13]).

Despite the fact that higher accuracy can be achieved, quantification of errors due to Lagrangian artifacts such as particle clustering is still an important issue. There are some techniques predicting numerical and modeling errors such as reported by Roache [21], Oden and Vemaganti [22], Afshar and Shobeyri [23] and many others. Employment of method of posteriori error approximation for prediction of errors induced by particle clustering seems to be possible. For this purpose, SPH discretization can be introduced to the weak formulation of Navier- Stokes equations. Then, an error equation for each flow variables can be constructed. At this stage, the difference between the evenly distributed and clustered particles should come into effect in error equation by introduction of a parameter. In this regard, a comparison between the Radial Distribution Functions of each system may be a very good candidate for determining the mentioned parameter. It should be noted that, the task of measuring errors itself is a very complicated task [24]. However, instead of this, the bounds of error can be identified theoretically by use of residual functionals [25]. The amount of error between evenly distributed and disordered particles can be quantified by an Energy norm, such as given by Ciarlet [26].

In this thesis, Incompressible SPH method is implemented to simulate a wide range of problems which can be classified by isothermal, nonisothermal, double-diffusive and two-phase flows. For isothermal flows, vortex spin-down and lid-driven cavity problems are studied. Moreover, for non-isothermal flows, energy equation with a proper projection scheme is implemented to the isothermal ISPH coded and natural convection is investigated. In natural convection case, three different problems are considered. In the first natural convection case, classical natural convection in a square cavity problem is simulated. For this case, a grid-based ISPH approach is proposed instead of the conventional SPH approaches. Grid-based ISPH approach is only applied to the first natural convection case. In the second natural convection case, Rayleigh-Bénard convection is simulated and multiple states of the solutions are discussed. In the third natural convection case, natural convection is at the onset of instability is studied. Furthermore, double-diffusion is investigated with the addition of mass transfer equation to the ISPH code with a proper projection scheme. Finally, two-phase flow is studied in terms of topological changes of interfaces and Rayleigh-Taylor

instability, and results obtained by ISPH and Level Set method are compared.

In the context of grid-based ISPH technique, as opposed to conventional SPH approaches, SPH particles are kept stationary. The aim is to test the upper limit of accuracy of SPH computations. Since all particles are stationary, Eulerian form of governing equations is used instead of Lagrangian form of governing equations. Incompressible SPH (ISPH) method is used to simulate transient and laminar natural convection in square cavity with Boussinesq approximation. For solid boundary modeling, mirror particle approach presented by in Morris *et al.* [5] is implemented.

The most important advantage of grid-based ISPH approach is that density field is kept constant and uniformity of particle distribution is guaranteed during simulations. In other words, this approach presented prevents density error accumulation and particle disorder, which are reported as limiting factors of the capacity of ISPH method. Since constant density field and uniform particle distribution increases the accuracy of kernel approximations, grid-based ISPH method can be deduced to be the upper limit of SPH computations.

However, grid-based ISPH naturally loses some advantages of Lagrangian SPH. For instance, Lagrangian applications of SPH in multiphase flows do not require any additional process to model interfaces. By its nature, Lagrangian SPH handles interfaces automatically. On the other hand, many Eulerian methods (e.g. PIC, MAC, VOF, Level set method etc.) can model multiphase flows (e.g. Ren *et al.* [27]) but these methods introduce either additional equations or models. Similarly, this approach requires such an additional tool to model interface. However, the goal of grid-based ISPH technique is to test the upper limit of accuracy of SPH simulation. Therefore, this approach mainly focuses on preventing fundamental causes of errors in Lagrangian SPH simulation (density error and particle disorder) rather than proposing a general approach of application although this is possible as in many Eulerian methods.

2. SPH Methodology

SPH is derived from integral representation of any scalar function, $f(\mathbf{r})$, defined on a three dimensional coordinate system using Dirac delta function:

$$f(\mathbf{r}) = \int_{\forall} f(\mathbf{r}')\delta(\mathbf{r} - \mathbf{r}')\, d\mathbf{r}' \tag{2.1}$$

where $\delta(\mathbf{r} - \mathbf{r}')$ is Dirac delta function and $\forall$ is the volume over which $d\mathbf{r}'$ is ranging. Dirac delta function, $\delta(\mathbf{r} - \mathbf{r}')$, is approximated by a smoothing kernel $W(\mathbf{r} - \mathbf{r}', h)$

$$\delta(\mathbf{r} - \mathbf{r}') = \lim_{h \to 0} W(\mathbf{r} - \mathbf{r}', h) \tag{2.2}$$

where h is the smoothing length that confines neighborhood of particles. Smoothing kernel, $W(\mathbf{r} - \mathbf{r}', h)$, is subjected to normalization condition :

$$\int_{\forall} W(\mathbf{r} - \mathbf{r}', h)\, d\mathbf{r}' = 1 \tag{2.3}$$

For symmetric smoothing kernels, $W(\mathbf{r}-\mathbf{r}', h) = W(\mathbf{r}'-\mathbf{r}, h)$, by expanding $W(\mathbf{r}-\mathbf{r}', h)$ in Taylor series, Equation 2.1 can be approximated as

$$f(\mathbf{r}) = \int_{\forall} f(\mathbf{r}')W(\mathbf{r} - \mathbf{r}', h)\, d\mathbf{r}' + \mathcal{O}(h^2) \tag{2.4}$$

Multiplying and dividing the integrand in Equation 2.4 by density $\rho(\mathbf{r}')$, an equivalent expression to Equation 2.4 is obtained

$$f(\mathbf{r}) = \int_{\forall} \frac{f(\mathbf{r}')}{\rho(\mathbf{r}')} W(\mathbf{r} - \mathbf{r}', h)\, \rho(\mathbf{r}')d\mathbf{r}' + \mathcal{O}(h^2) \tag{2.5}$$

Since SPH discretizes a continuum onto a set of particles of mass $m' = \rho(r')dr'$ Equation

2.5 becomes the famous SPH summation formula

$$f_i = \sum_j \frac{m_j}{\rho_j} f_j W_{ij} \tag{2.6}$$

where $f_i = f(\mathbf{r}_i)$, $W_{ij} = W(\mathbf{r}_i - \mathbf{r}_j, h)$ and any difference of a certain parameter, f, corresponding to two different particle is shown using the notation $f_{ij} = f_i - f_j$. A function can be calculated at a particle i using Equation 2.6. For instance, density of a particle i is calculated as;

$$\rho_i = \sum_j m_j W_{ij} \tag{2.7}$$

In this thesis, quintic kernel due to Schoenberg [28] is used since it is frequently used in SPH literature.

$$W_{ij} = \frac{3}{478\pi} \begin{cases} (3-q)^5 - 6(2-q)^5 + 15(1-q)^5, & 0 \leq q \leq 1 \\ (3-q)^5 - 6(2-q)^5 & 1 \leq q \leq 2 \\ (3-q)^5 & 2 \leq q \leq 3 \\ 0 & 3 \leq q \end{cases} \tag{2.8}$$

where $q = \frac{r_{ij}}{h}$. A comprehensive discussion on effect of kernel types and properties, especially on particle disorder, can be found in [29].

Moreover, SPH can be used to discretize mathematical operators such as derivative, divergence, gradient and laplacian operators. In the following sections, SPH discretization of these operators are discussed.

2.1. SPH Form of Mathematical Operators

Governing equations describing a physical phenomenon usually include mathematical operators such as derivative, gradient, divergence and laplacian operators. Like other computational methods, SPH can approximate these operators.

2.1.1. SPH Derivative Operator

SPH derivative operator is obtained from differentiating Equation 2.4

$$\frac{\partial}{\partial r} f(\mathbf{r}) = \frac{\partial}{\partial r} \int_{\forall} f(\mathbf{r}') W(\mathbf{r} - \mathbf{r}', h)\, d\mathbf{r}' \tag{2.9}$$

$$= \int_{\forall} f(\mathbf{r}') \frac{\partial W(\mathbf{r} - \mathbf{r}', h)}{\partial r}\, d\mathbf{r}' \tag{2.10}$$

Discretizing Equation 2.9 similar to Equation 2.4, SPH derivative operator is obtained as

$$\frac{\partial f_i}{\partial r_i} = \sum_j \frac{m_j}{\rho_j} f_j \frac{\partial W_{ij}}{\partial r_i} \tag{2.11}$$

Furthermore, smoothing kernel must be a normalized function

$$1 = \sum_j \frac{m_j}{\rho_j} W_{ij} \tag{2.12}$$

Then, derivative of "1" is calculated as

$$0 \approx \frac{\partial(1)}{\partial r_i} = \sum_j \frac{m_j}{\rho_j} \frac{\partial W_{ij}}{\partial r_i} \tag{2.13}$$

Therefore, there is an error associated with the derivative of a constant function. Thus, considering

$$\frac{\partial(f \cdot 1)}{\partial r} = \frac{\partial(f)}{\partial r} \cdot 1 + \frac{\partial 1}{\partial r} \cdot f \tag{2.14}$$

$$\frac{\partial f}{\partial r} = \frac{\partial f}{\partial r} - \frac{\partial 1}{\partial r}. \tag{2.15}$$

accuracy of SPH derivative operator is increased by taking the errors associated with the derivative of "1" into account

$$\frac{\partial f_i}{\partial r_i} = \sum_j \frac{m_j}{\rho_j} (f_j - f_i) \frac{\partial W_{ij}}{\partial r_i} \tag{2.16}$$

This procedure can be generalized by differentiation $\frac{\partial}{\partial r}(f\rho^n) = \rho^n \frac{\partial f}{\partial r} + nf\rho^{n-1}\frac{\partial \rho}{\partial r}$. Thus,

$$\frac{\partial f_i}{\partial r_i} = \frac{1}{\rho_i^n}\left(\frac{\partial}{\partial r_i}(f_i\rho_i^n) - nf_i\rho_i^{n-1}\frac{\partial \rho_i}{\partial r_i}\right) \tag{2.17}$$

$$= \frac{1}{\rho_i^n}\sum_j \frac{m_j}{\rho_j}\left(f_j\rho_j^n - nf_i\rho_i^{n-1}\rho_j\right)\frac{\partial W_{ij}}{\partial r_i} \tag{2.18}$$

Two commonly used SPH derivative operators are obtain for $n = 1$ and $n = -1$. For $n = 1$, SPH derivative operator becomes

$$\frac{\partial f_i}{\partial r_i} = \frac{1}{\rho_i}\sum_j m_j\left(f_j - f_i\right)\frac{\partial W_{ij}}{\partial r_i} \tag{2.19}$$

For $n = -1$, SPH derivative operator becomes

$$\frac{\partial f_i}{\partial r_i} = \rho_i \sum_j m_j\left(\frac{f_i}{\rho_i^2} + \frac{f_j}{\rho_j^2}\right)\frac{\partial W_{ij}}{\partial r_i} \tag{2.20}$$

For a constant function, Equation 2.19 results in identically "0" while Equation 2.20 does not. In this study, Equation 2.19 is used.

2.1.2. SPH Gradient Operator

Similar to SPH derivative operator, there are two types of SPH gradient operators commonly used in SPH literature [4, 5, 11, 13, 20].

$$(\nabla f)_i = \frac{1}{\rho_i}\sum_j m_j\left(f_j - f_i\right)\nabla_i W_{ij} \tag{2.21}$$

$$(\nabla f)_i = \rho_i \sum_j m_j\left(\frac{f_i}{\rho_i^2} + \frac{f_j}{\rho_j^2}\right)\nabla_i W_{ij} \tag{2.22}$$

In SPH literature, Equation 2.22 is commonly used in discretization of pressure gradient term since this operator is symmetric and conserves linear momentum. However, Equation 2.21 is used in this study. Although Equation 2.21 does not conserve linear momentum, it results in more accurate approximations than Equation 2.22.

2.1.3. SPH Divergence Operator

Likewise SPH gradient operator, SPH divergence operator can be constructed as follows [4, 5, 11, 13, 20].

$$(\nabla \cdot \mathbf{f})_i = \frac{1}{\rho_i} \sum_j m_j (\mathbf{f}_j - \mathbf{f}_i) \cdot \nabla_i W_{ij} \tag{2.23}$$

$$(\nabla \cdot \mathbf{f})_i = \rho_i \sum_j m_j \left(\frac{\mathbf{f}_i}{\rho_i^2} + \frac{\mathbf{f}_j}{\rho_j^2} \right) \cdot \nabla_i W_{ij} \tag{2.24}$$

In this study, Equation 2.23 is used.

2.1.4. SPH Laplacian Operator

Laplacian operator usage differs from gradient and divergence operators in SPH literature [4, 5, 11, 13, 20]. The simplest SPH Laplacian operator is

$$\left(\nabla^2 f\right)_i = \sum_j \frac{m_j}{\rho_j} f_j \nabla^2 W_{ij} \tag{2.25}$$

Another form of SPH Laplacian operator is called *"Approximate Laplacian operator"*.

$$\left(\nabla^2 f\right)_i = \sum_j 2 \frac{m_j}{\rho_j} \frac{\mathbf{r}_{ij} \cdot \nabla W_{ij}}{|\mathbf{r}_{ij}|^2 + \eta^2} f_{ij} \tag{2.26}$$

where η is a very small number in order to prevent a zero denominator. Approximate Laplacian operator was first used in [30] and it is one of the most commonly used SPH Laplacian operators. It combines finite difference and SPH derivative operators. A more general form of Equation 2.26 is given as [20]

$$\nabla \cdot (k \nabla f)_i = \sum_{j \neq i} \frac{m_j}{\rho_j} (k_i + k_j) \frac{r_{ij} \cdot \nabla W_{ij}}{|r_{ij}|^2} f_{ij} \tag{2.27}$$

and Equation 2.27 is the Laplacian operator used in this thesis.

2.2. High Order Approximation Schemes in SPH

In Lagrangian SPH approach, one of the most significant problems is that uniformity of particle distribution is not conserved exactly during simulations. As a consequence, inaccuracies arise as kernel and its derivatives are discretized. In order to remedy these, correction techniques for kernel and its derivatives were developed [31–34]. An instructive summary of these techniques are presented in [35] and [6].

In the proceeding subsection, correction methods used in SPH method are given systematically and behavior of those corrections on uniformly distributed grids will be discussed in detail.

2.2.1. Density Field Correction

Shepard Filter: This is a "zeroth order" correction technique. It is very simple to implement. It is based on normalization on smoothing kernel W. In SPH, density of a particle is calculated by

$$\rho_i = \sum_j m_j W_{ij} \tag{2.28}$$

However, smoothing kernel usually does not satisfy the normalization condition

$$1 = \sum_j \frac{m_j}{\rho_j} W_{ij} \tag{2.29}$$

As a consequence, density field calculated by Equation 2.28 is inaccurate. In order to increase accuracy of density field, a corrected smoothing kernel is calculated by

$$\tilde{W}_{ij} = \frac{W_{ij}}{\sum_k \frac{m_k}{\rho_k} W_{ik}} \tag{2.30}$$

Then, corrected density field is calculated by inserting corrected smoothing kernel $\tilde{W}_{ij}$ into Equation 2.29

$$\rho_i^{corrected} = \sum_j m_j \tilde{W}_{ij} \tag{2.31}$$

NOTE: In Grid-Based SPH, Equation 2.29 holds exactly. Therefore, denominator in Equation 2.30 is equal to 1. Therefore, following relation holds:

$$\tilde{W}_{ij} = W_{ij} \tag{2.32}$$

As a consequence, $\rho_i^{corrected}$ and ρ_i are identical:

$$\rho_i^{corrected} = \rho_i \tag{2.33}$$

Thus, in Grid-based SPH, usage of Shepard filter is unnecessary.

Moving Least Squares(MLS): This is a first order correction approach. It is similar to Shepard filter in terms of calculating a new smoothing kernel W_{ij}^{MLS}.

$$\rho_i = \sum_j m_j W_{ij}^{MLS} \tag{2.34}$$

where W_{ij}^{MLS} is calculated by

$$W_{ij}^{MLS} = \vec{\beta} \cdot (\vec{r}_i - \vec{r}_j) W_{ij} \tag{2.35}$$

In Equation 2.35, $\vec{\beta}$ is a vector estimated by

$$\vec{\beta} = \begin{bmatrix} \beta_1 \\ \beta_2 \\ \beta_3 \end{bmatrix} = \mathbf{A}^{-1} \begin{bmatrix} 1 \\ 0 \\ 0 \end{bmatrix} \tag{2.36}$$

and $\mathbf{A}$ is a matrix obtained by

$$\mathbf{A} = \sum_j \frac{m_j}{\rho_j} \tilde{\mathbf{A}} W_{ij} \tag{2.37}$$

where $\tilde{\mathbf{A}}$ is

$$\tilde{\mathbf{A}} = \begin{bmatrix} 1 & (x_i - x_j) & (y_i - y_j) \\ (x_i - x_j) & (x_i - x_j)^2 & (x_i - x_j)(y_i - y_j) \\ (y_i - y_j) & (x_i - x_j)(y_i - y_j) & (y_i - y_j)^2 \end{bmatrix} \tag{2.38}$$

For a 2D problem, W_{ij}^{MLS} is calculated by

$$W_{ij}^{MLS} = (\beta_1 + \beta_2(x_i - x_j) + \beta_3(y_i - y_j))\, W_{ij} \tag{2.39}$$

NOTE: In Grid-based SPH, $\mathbf{A}$ is calculated by using a normalized symmetric kernel W_{ij}. Therefore,

$$\begin{aligned}
\mathbf{A}_{11} &= \textstyle\sum_j \frac{m_j}{\rho_j} W_{ij} = 1 \\
\mathbf{A}_{12} &= \textstyle\sum_j \frac{m_j}{\rho_j} (x_i - x_j)\, W_{ij} = 0 \\
\mathbf{A}_{13} &= \textstyle\sum_j \frac{m_j}{\rho_j} (y_i - y_j)\, W_{ij} = 0 \\
\mathbf{A}_{21} &= \textstyle\sum_j \frac{m_j}{\rho_j} (x_i - x_j)\, W_{ij} = 0 \\
\mathbf{A}_{22} &= \textstyle\sum_j \frac{m_j}{\rho_j} (x_i - x_j)^2\, W_{ij} \neq 0 \\
\mathbf{A}_{23} &= \textstyle\sum_j \frac{m_j}{\rho_j} (x_i - x_j)(y_i - y_j)\, W_{ij} = 0 \\
\mathbf{A}_{31} &= \textstyle\sum_j \frac{m_j}{\rho_j} (y_i - y_j)\, W_{ij} = 0 \\
\mathbf{A}_{32} &= \textstyle\sum_j \frac{m_j}{\rho_j} (x_i - x_j)(y_i - y_j)\, W_{ij} = 0 \\
\mathbf{A}_{33} &= \textstyle\sum_j \frac{m_j}{\rho_j} (y_i - y_j)^2\, W_{ij} \neq 0
\end{aligned} \tag{2.40}$$

Therefore, $\mathbf{A}$ is obtained as

$$\mathbf{A} = \begin{bmatrix} 1 & 0 & 0 \\ 0 & c_1 & 0 \\ 0 & 0 & c_2 \end{bmatrix} \tag{2.41}$$

where c_1 and c_2 are some values estimated for $\mathbf{A}_{22}$ and $\mathbf{A}_{33}$. In order to calculate $\vec{\beta}$, inverse of $\mathbf{A}$ is to be calculated, which is a very simple task. Indeed,

$$\mathbf{A}^{-1} = \begin{bmatrix} 1 & 0 & 0 \\ 0 & d_1 & 0 \\ 0 & 0 & d_2 \end{bmatrix} \tag{2.42}$$

where d_1 and d_2 are values satisfying $c_1 \cdot d_1 = 1$ and $c_2 \cdot d_2 = 1$. Having obtained $\mathbf{A}^{-1}$, $\vec{\beta}$ can be calculated as

$$\vec{\beta} = \begin{bmatrix} 1 & 0 & 0 \\ 0 & d_1 & 0 \\ 0 & 0 & d_2 \end{bmatrix} \begin{bmatrix} 1 \\ 0 \\ 0 \end{bmatrix} = \begin{bmatrix} 1 \\ 0 \\ 0 \end{bmatrix} \tag{2.43}$$

Thus,

$$\begin{aligned} W_{ij}^{MLS} &= (\beta_1 + \beta_2(x_i - x_j) + \beta_3(y_i - y_j))\, W_{ij} \\ &= \beta_1\, W_{ij} \\ &= W_{ij} \end{aligned} \tag{2.44}$$

Thus, in Grid-Based SPH, MLS correction is unnecessary.

2.2.2. Kernel Correction

This is very similar to Shepard Filter. In SPH, a function f_i is calculated by

$$f_i = \sum_j \frac{m_j}{\rho_j} f_j W_{ij} \tag{2.45}$$

However, when particle consistency degrades, Equation 2.45 inaccurately approximates f_i. Therefore, Equation 2.45 is normalized by

$$f_i = \frac{\sum_j \frac{m_j}{\rho_j} f_j W_{ij}}{\sum_j \frac{m_j}{\rho_j} W_{ij}} \tag{2.46}$$

NOTE: In Grid-based SPH, since a normalized symmetric kernel W_{ij} is used, the following is obtained.

$$f_i = \frac{\sum_j \frac{m_j}{\rho_j} f_j W_{ij}}{\sum_j \frac{m_j}{\rho_j} W_{ij}} = \sum_j \frac{m_j}{\rho_j} f_j W_{ij} \tag{2.47}$$

Therefore, Kernel Correction is unnecessary in Grid-Based SPH.

2.2.3. Kernel Gradient Correction

Since governing equations of Fluid Mechanics involve terms including taking gradients, approximation of gradients is a significant task in terms of accuracy. In SPH, kernel gradients are used in calculation of gradients of terms in governing equations. However, when particle consistency degrades, conventional approaches in kernel gradient calculation produce errors. In order to prevent this, kernel gradient should be normalized. The normalized kernel gradient is calculated by

$$\nabla \tilde{W}_{ij} = \mathbf{L}^{-1} \nabla W_{ij} \tag{2.48}$$

where $\mathbf{L}$ is a matrix

$$\mathbf{L} = \begin{bmatrix} \sum_j \frac{m_j}{\rho_j}(x_j - x_i)\frac{\partial W_{ij}}{\partial x_i} & \sum_j \frac{m_j}{\rho_j}(x_j - x_i)\frac{\partial W_{ij}}{\partial y_i} \\ \sum_j \frac{m_j}{\rho_j}(y_j - y_i)\frac{\partial W_{ij}}{\partial x_i} & \sum_j \frac{m_j}{\rho_j}(y_j - y_i)\frac{\partial W_{ij}}{\partial y_i} \end{bmatrix} \tag{2.49}$$

See [34] for the basic idea in choosing $\mathbf{L}$.

NOTE: In Grid-Based SPH, L_{ij}'s become

$$\begin{aligned} L_{11} = \sum_j \frac{m_j}{\rho_j}(x_j - x_i)\frac{\partial W_{ij}}{\partial x_i} &= 1 \\ L_{12} = \sum_j \frac{m_j}{\rho_j}(x_j - x_i)\frac{\partial W_{ij}}{\partial y_i} &= 0 \\ L_{21} = \sum_j \frac{m_j}{\rho_j}(y_j - y_i)\frac{\partial W_{ij}}{\partial x_i} &= 0 \\ L_{22} = \sum_j \frac{m_j}{\rho_j}(y_j - y_i)\frac{\partial W_{ij}}{\partial y_i} &= 1 \end{aligned} \tag{2.50}$$

In matrix representation, $\mathbf{L}$ is obtained as

$$\mathbf{L} = \begin{bmatrix} 1 & 0 \\ 0 & 1 \end{bmatrix} \tag{2.51}$$

which is the identity matrix. Inserting this into Equation 2.48, the following is obtained,

$$\nabla \tilde{W}_{ij} = \nabla W_{ij} \tag{2.52}$$

As a conclusion, kernel gradient correction technique is unnecessary in Grid-Based SPH technique as in previous correction techniques. It is worthwhile to note that ineffectiveness of these correction techniques in grid-Based SPH is independent of kernel types and properties. Therefore, kernel types and properties do not have any effect on the results except for discretization error. However, in conventional SPH techniques, kernel type and properties have influences on particle disorder and thus, they have significant effect on the results [29].

2.3. Pressure Projection in SPH

In literature, there are several ISPH techniques that depend on pressure projection method [8–13, 15]. These ISPH approaches are commonly implemented to solve isothermal flow equations. Except for a few example, non-isothermal and double diffusive applications are not studied by ISPH techniques in detail. In this thesis, ISPH technique is extended to non-isothermal and double diffusive flows.

In the most general form of an incompressible flow problem including momentum, energy and mass transport, governing equations are continuity, momentum, energy and

mass transfer equations given respectively as

$$\frac{1}{\rho}\frac{D\rho}{Dt} = -\nabla\cdot\vec{u} = 0 \tag{2.53}$$

$$\frac{D\vec{u}}{Dt} = -\frac{1}{\rho}\nabla p + \frac{1}{\rho}\nabla\cdot(\mu\nabla\vec{u}) + \vec{f} \tag{2.54}$$

$$\frac{DT}{Dt} = \alpha\nabla^2 T \tag{2.55}$$

$$\frac{DC}{Dt} = D\nabla^2 C \tag{2.56}$$

where ρ is density, $\vec{u}$ is velocity, p is pressure, μ is dynamic viscosity, $\vec{f}$ is a body force, T is temperature, C is concentration, α is thermal diffusivity and D is solutal diffusivity. From Equation 2.53, two different incompressibility conditions are obtained.

$$\frac{1}{\rho}\frac{D\rho}{Dt} = 0 \tag{2.57}$$

$$\nabla\cdot\vec{u} = 0 \tag{2.58}$$

In ISPH technique used in this thesis, intermediate values of velocity, temperature and concentration are calculated at the position $\vec{r}^n$.

$$\vec{u}^* = \vec{u}^n + \Delta t\left(\frac{1}{\rho^n}\nabla\cdot(\mu\nabla\vec{u}^n) + \vec{f}^n\right) \tag{2.59}$$

$$T^{n+1/2} = T^n + \Delta t(\alpha\nabla^2 T^n) \tag{2.60}$$

$$C^{n+1/2} = C^n + \Delta t(D\nabla^2 C^n) \tag{2.61}$$

It should be noted that pressure gradient term in Equation 2.54 is not included in Equation 2.59. Moreover, particle positions at the intermediate half-step are calculated using $\vec{u}^*$.

$$\vec{r}^* = \vec{r}^n + \Delta t\,\vec{u}^* \tag{2.62}$$

Since $\vec{r}^*$ does not correspond to a physical intermediate time step, intermediate values of temperature and concentration are denoted by $n + 1/2$. Then, velocity at the new

time step is estimated by

$$\vec{u}^{n+1} = \vec{u}^{*} - \frac{\Delta t}{\rho^{*}} \nabla p^{n+1} \tag{2.63}$$

However, before obtaining $\vec{u}^{n+1}$, pressure p^{n+1} must be calculated. By applying divergence operator to Equation 2.63 and considering incompressibility condition in Equation 2.53, pressure Poisson equation is obtained as

$$\nabla \cdot \left(\frac{1}{\rho^{*}} \nabla p^{n+1} \right) = \frac{1}{\Delta t} \nabla \cdot u^{*} \tag{2.64}$$

Using Equation 2.58, the term $\nabla \cdot u^{*}$ can also be written as

$$\nabla \cdot u^{*} = -\frac{1}{\rho} \frac{D\rho}{Dt} \approx \frac{\rho^{n} - \rho^{*}}{\rho^{n} \Delta t} \tag{2.65}$$

Then, Equation 2.64 becomes

$$\nabla \cdot \left(\frac{1}{\rho^{*}} \nabla p^{n+1} \right) = \frac{\rho^{n} - \rho^{*}}{\rho^{n} \Delta t^{2}} \tag{2.66}$$

After solving for pressure p^{n+1}, velocity at the next time step $\vec{u}^{n+1}$ is calculated. Then, new particles are moved to the new position according to

$$\vec{r}^{n+1} = \vec{r}^{n} + \Delta t \left(\frac{\vec{u}^{n+1} + \vec{u}^{n}}{2} \right) \tag{2.67}$$

Finally, at the new positions, temperature and concentration are calculated as

$$T^{n+1} = T^{n} + \alpha \Delta t \left(\frac{\nabla^{2} T^{n+1} + \nabla^{2} T^{n}}{2} \right) \tag{2.68}$$

$$C^{n+1} = C^{n} + D \Delta t \left(\frac{\nabla^{2} C^{n+1} + \nabla^{2} C^{n}}{2} \right) \tag{2.69}$$

It should be noted that $\nabla^{2} T^{n}$ and $\nabla^{2} C^{n}$ values are calculated at the particle position $\vec{r}^{n}$ while $\nabla^{2} T^{n+1}$ and $\nabla^{2} C^{n+1}$ values are calculated at the particle position $\vec{r}^{n+1}$.

3. MODEL PROBLEMS

In this thesis, ISPH technique is applied to several convective-diffusive transport problems. In each problem, 2D incompressible Newtonian flow is considered. The problems can be classified by isothermal flow, non-isothermal flow, non-isoconcentration flow and two-phase flow. In isothermal flow case, lid-driven cavity and vortex spin-down problems are simulated. Moreover, in non-isothermal flow case, natural convection in a cavity problem is investigated. In non-isoconcentration flow case, double-diffusive transport is studied. Lastly, in two-phase flow case, rising bubble, droplet fall, bursting bubble at the free surface, droplet fall onto the free surface and Rayleigh-Taylor instability problems are considered.

3.1. Lid-driven Cavity

Lid-driven cavity is a well known benchmark problem and it is one of the isothermal problems used for validation of ISPH code developed in this thesis. Flow is considered on the horizontal plane such that effects of gravitational acceleration are neglected. Lid is driven by a constant velocity, U_0, during simulations as shown in Figure 3.1. Moreover, incompressibility is enforced by applying Equation 3.1 and Navier-Stokes equations in Equation 3.2 are solved using ISPH projection method discussed in Section 2.3.

$$\nabla \cdot \vec{u} = 0 \tag{3.1}$$

$$\frac{D\vec{u}}{Dt} = -\frac{1}{\rho}\nabla p + \frac{1}{\rho}\nabla \cdot (\mu \nabla \vec{u}) \tag{3.2}$$

Since fluid is Newtonian and isothermal, kinematic viscosity, $\nu = \mu/\rho$, is constant. Therefore, viscous term in Equation 3.2 is rewritten as $\nu/\rho\nabla \cdot (\rho\nabla\vec{u})$. Although an incompressible fluid model is considered, particles cannot be distributed uniformly due to meshfree nature of SPH. For this reason, density field, ρ, shows small oscillations around a reference density, ρ_0 and is not taken out of differential terms.

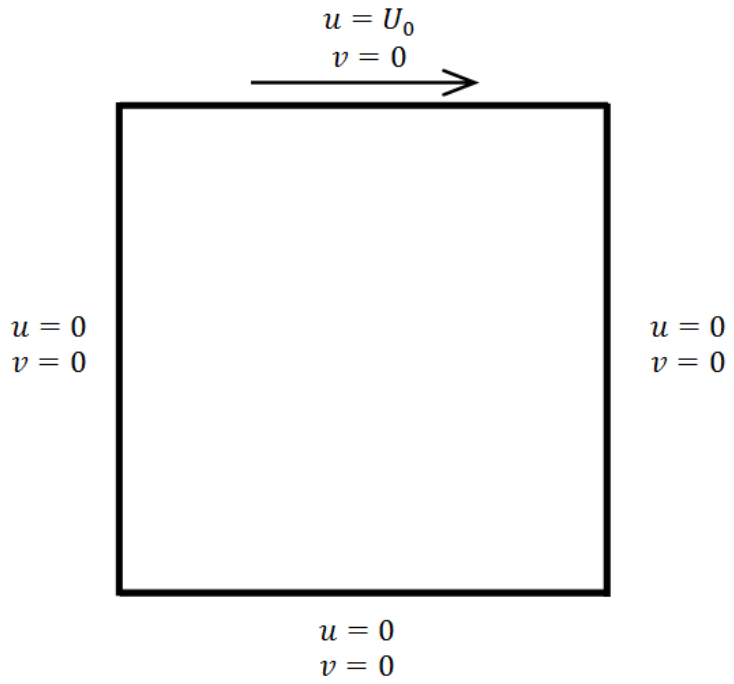

Figure 3.1. Problem geometry and boundary conditions for lid-driven cavity problem.

3.2. Vortex Spin-down

Vortex spin-down is another isothermal problem used for validation of ISPH code. As in lid-driven cavity problem in Section 3.1, flow is considered on the horizontal plane such that effects of gravitational acceleration are neglected. All velocity components are equal to zero at all walls and an initial rotation is given as shown in Figure 3.2. The initial velocity field is

$$\begin{aligned} u &= U_0(y - 0.5) \\ v &= U_0(0.5 - x) \end{aligned} \tag{3.3}$$

where U_0 is a characteristics velocity. Similar to lid-driven cavity problem, projection method discussed in 2.3 is employed by enforcing incompressibility condition in Equation 3.4 to solve Navier-Stokes equations in Equation 3.5.

$$\nabla \cdot \vec{u} = 0 \tag{3.4}$$

$$\frac{D\vec{u}}{Dt} = -\frac{1}{\rho}\nabla p + \frac{1}{\rho}\nabla \cdot (\mu \nabla \vec{u}) \tag{3.5}$$

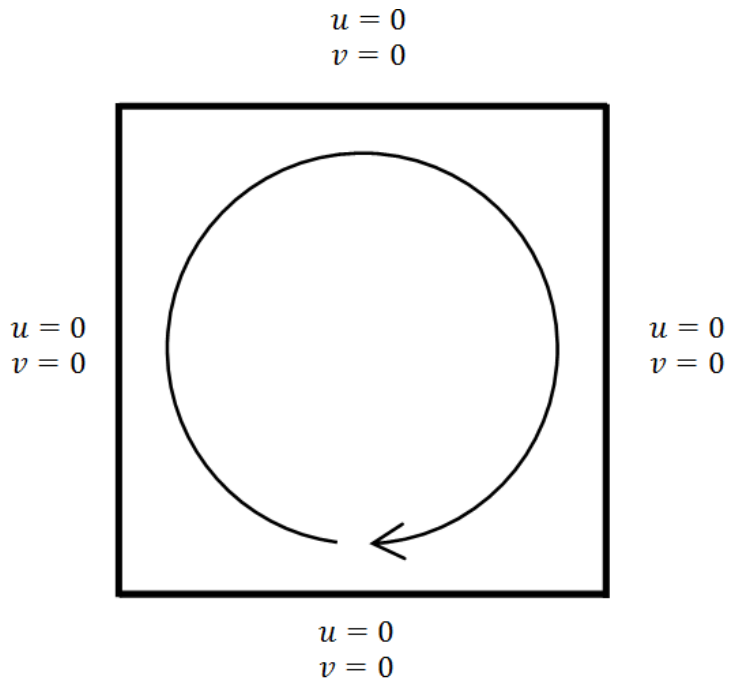

Figure 3.2. Problem geometry and boundary conditions for vortex spin-down problem.

Furthermore, viscous term in Equation 3.5 is treated in the same way as in lid-driven cavity problem. Therefore, viscous term is rewritten as $\nu/\rho\nabla\cdot(\rho\nabla\vec{u})$.

3.3. Natural Convection

Natural convection is an important problem of non-isothermal flow. In addition to the continuity and Navier-Stokes equations, energy equation is required to be solved.

$$\nabla\cdot\vec{u} = 0 \tag{3.6}$$

$$\frac{D\vec{u}}{Dt} = -\frac{1}{\rho}\nabla\tilde{p} + \frac{1}{\rho}\nabla\cdot(\mu\nabla\vec{u}) + \vec{g} \tag{3.7}$$

$$\frac{DT}{Dt} = \alpha\nabla^2 T \tag{3.8}$$

Equation 3.7 is usually simplified by separating the pressure gradient due to hydrostatic pressure field from pressure gradient term such that

$$\nabla\tilde{p} = \nabla p + \rho_0\vec{g} \tag{3.9}$$

where ρ_0 is a reference density. Moreover, rewriting Equation 3.7, the following form of momentum equation is obtained.

$$\frac{D\vec{u}}{Dt} = -\frac{1}{\rho}\nabla p + \frac{1}{\rho}\nabla \cdot (\mu \nabla \vec{u}) + \left(1 - \frac{\rho_0}{\rho}\right)\vec{g} \tag{3.10}$$

In general, a further simplification is made by employing Boussinesq approximation according to which every variable is assumed to be constant except body forces. Therefore, density variation is allowed. In order to estimate density variation, density is expanded in Taylor series.

$$\rho = \rho_0 + \left(\frac{\partial \rho}{\partial T}\right)_P (T - T_0) + \left(\frac{\partial \rho}{\partial P}\right)_T (P - P_0) + \dots \tag{3.11}$$

Since density is considered to be a function of temperature only, $\rho = \rho(T)$, in natural convection problems, the last term is neglected. Lastly, volumetric coefficient of thermal expansion is introduced.

$$\beta = -\frac{1}{\rho}\left(\frac{\partial \rho}{\partial T}\right)_P \tag{3.12}$$

Then, a simpler equation for density variation is obtained.

$$\rho - \rho_0 = -\rho\beta(T - T_0) \tag{3.13}$$

Inserting Equation 3.32 into Equation 3.10 and assuming gravity is in the negative y-direction, the following form of the momentum equation is obtained.

$$\frac{D\vec{u}}{Dt} = -\frac{1}{\rho}\nabla p + \frac{1}{\rho}\nabla \cdot (\mu \nabla \vec{u}) + g\beta(T - T_0)\hat{j} \tag{3.14}$$

Finally, continuity, momentum and energy equations are non-dimensionalized.

$$(x^*, y^*) = \frac{(x, y)}{L} \tag{3.15}$$

$$\vec{u^*} = \vec{u}\frac{L}{\alpha} \tag{3.16}$$

$$t^* = t\frac{\alpha}{L^2} \tag{3.17}$$

$$T^* = \frac{T - T_C}{T_H - T_C} \tag{3.18}$$

$$p^* = p\frac{L^2}{\rho_0 \alpha^2} \tag{3.19}$$

$$\rho^* = \frac{\rho}{\rho_0} \tag{3.20}$$

$$Pr = \frac{\nu}{\alpha} \tag{3.21}$$

$$Ra = \frac{g\beta\,(T_H - T_C)\,L^3}{\nu\,\alpha} \tag{3.22}$$

where L is a characteristic length, T_H is the maximum temperature, T_C is the minimum temperature, Pr is Prandtl number, Ra is Rayleigh number. Then, the following form of governing equations are obtained.

$$\nabla \cdot \vec{u^*} = 0 \tag{3.23}$$

$$\frac{D\vec{u^*}}{Dt^*} = -\frac{1}{\rho^*}\nabla p^* + Pr\left(\frac{1}{\rho^*}\nabla \cdot (\rho^* \nabla \vec{u^*})\right) + PrRa(T^* - 0.5)\hat{\jmath} \tag{3.24}$$

$$\frac{DT^*}{Dt^*} = \nabla^2 T^* \tag{3.25}$$

Although WCSPH applications exist in literature, natural convection has been rarely studied by ISPH. Therefore, in this thesis, the projection method is extended for non-isothermal problems. The projection method for non-isothermal flow is discussed in Section 2.3. Employing the projection method, Equations 3.23, 3.24 and 3.25 are solved.

In this thesis, natural convection is studied by examining effect of several parameters such as Ra number, aspect ratio, boundary conditions and initial conditions. Accordingly, natural convection is investigated under three sub-categories. These categories are “Natural convection in a square cavity”, “Rayleigh-Bénard Convection” and

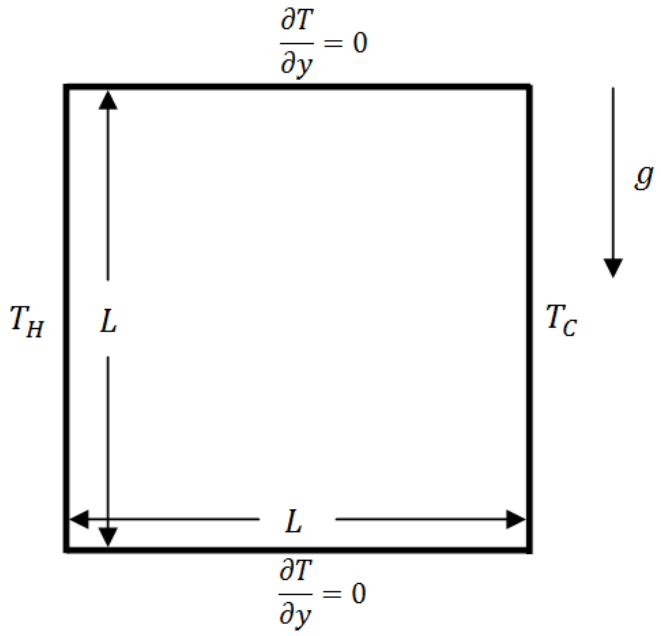

Figure 3.3. Problem geometry and boundary conditions for natural convection in a cavity problem.

"Natural convection at the onset of instability" and they are discussed in the following subsections.

3.3.1. Natural Convection in a Square Cavity

Natural convection in a square cavity is one of the most commonly used benchmark problems. This problem is named after the work of de Vahl Davis in 1983 [36]. Temperature is constant at side walls and the top and bottom walls are insulated as depicted in Figure 3.3. Mathematically, $T_H = 1$ at the left wall, $T_C = 0$ at the right wall and $\partial T/\partial y = 0$ at the bottom and top wall.

Initially, there is zero-velocity field and temperature field linearly varies from hot wall to the cold wall. In this problem, effect of Ra number is investigated and the results are compared with available data in literature.

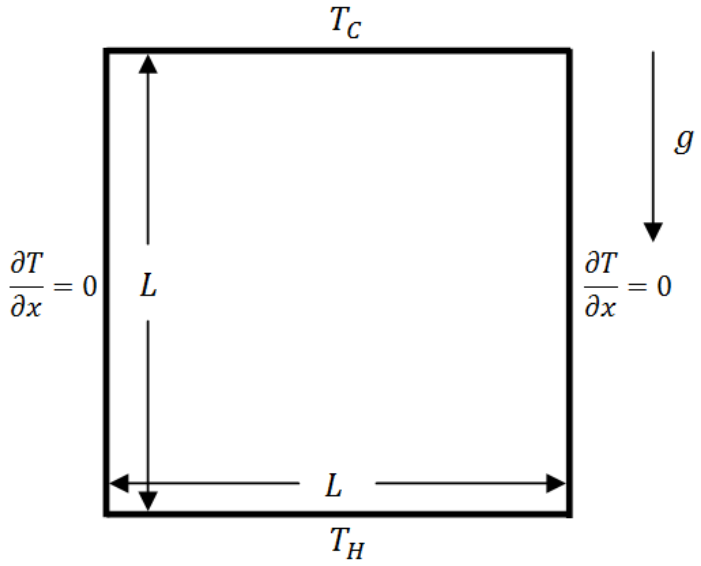

Figure 3.4. Problem geometry and boundary conditions for Rayleigh-Bénard problem.

3.3.2. Rayleigh-Bénard Convection

In Rayleigh-Bénard convection problem, temperature boundary conditions are changed. Temperature is constant at the top and bottom walls are insulated as depicted in Figure 3.4. Mathematically, $T_H = 1$ at the bottom wall, $T_C = 0$ at the top wall and $\partial T/\partial x = 0$ at the size walls.

It should be noted that multiple states of solution are possible in Rayleigh-Bénard convection. For the methods that solve the steady state equations, one of the multiple state is favored. SPH, being a meshless method, is applied to time dependent problems in general. Therefore, initial conditions are of great significance in this regard. Depending on the initial conditions, it is possible to obtain different solutions. In other words, different initial conditions may favor different state of solution. In the present study, it is shown that different initial conditions lead to different cellular structures and temperature profiles.

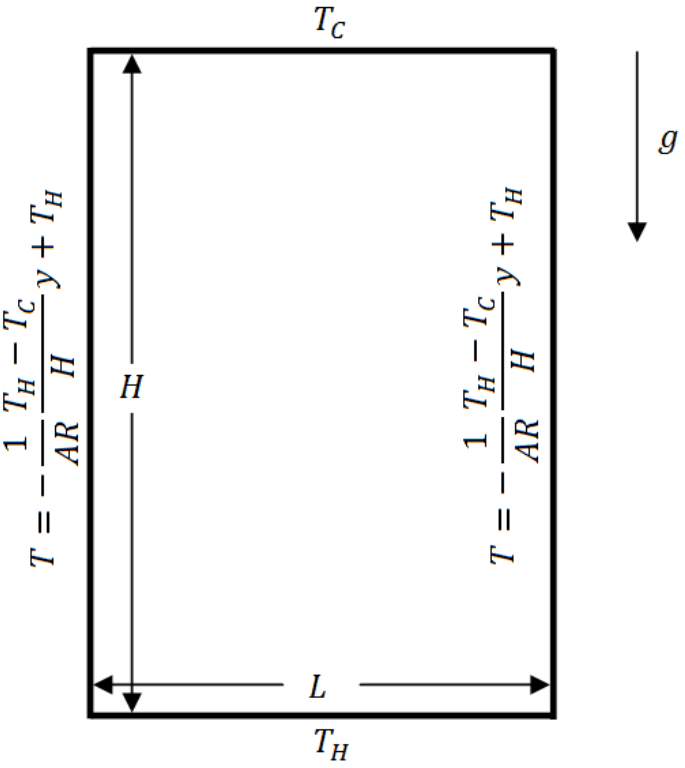

Figure 3.5. Problem geometry and boundary conditions for oscillatory natural convection problem.

3.3.3. Natural Convection at the Onset of Instability

Another non-isothermal case studied in this thesis is the natural convection at the onset of instability. In this problem, all temperature boundary conditions are of Dirichlet kind. As shown in Figure 3.5, $T_H = 1$ at the bottom wall, $T_C = 1$ at the top wall and temperature varies linearly from bottom wall to the top.

In this problem, effect of aspect ratio, $AR = H/L$, on the stability of flow is investigated for different velocity initial conditions. Regardless of the initial conditions, it is shown that behavior of flow is dependent on aspect ratio. Different cellular structures and heat transfer characteristics are observed for different aspect ratios.

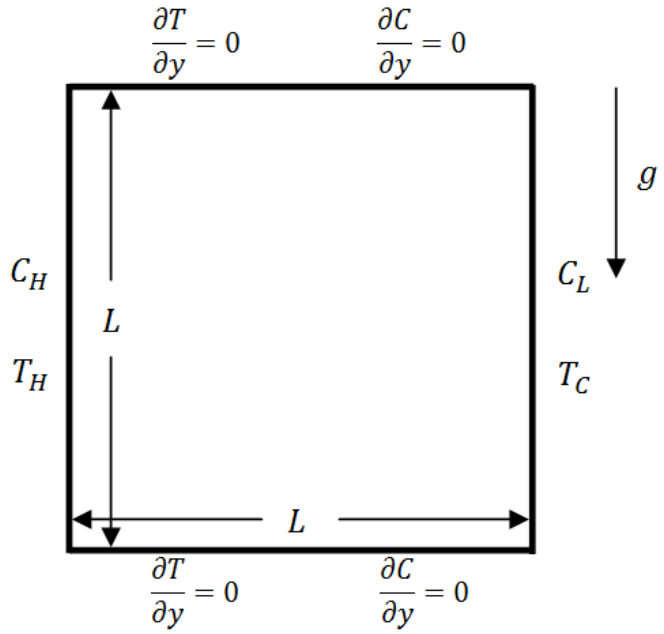

Figure 3.6. Problem geometry and boundary conditions for double diffusion problem.

3.4. Double-Diffusive Transport

Double-diffusion is the example of non-isoconcentration flow in this thesis. In addition to the momentum and energy, mass is transported in double-diffusion problems. For temperature and concentration, homogeneous Neumann boundary condition is applied at the top and bottom walls and Dirichlet boundary condition is applied at the side walls in this study. Mathematically, $T_H = 1$ and $C_H = 1$ at the left wall, $T_C = 0$ and $C_L = 0$ at the right wall, $\partial T/\partial y = 0$ and $\partial C/\partial y = 0$ at the bottom and top walls as seen in Figure 3.4.

In addition to Equations 3.6, 3.7 and 3.8, mass transfer equation is solved. Following is the complete set of equations.

$$\nabla \cdot \vec{u} = 0 \tag{3.26}$$

$$\frac{D\vec{u}}{Dt} = -\frac{1}{\rho}\nabla\tilde{p} + \frac{1}{\rho}\nabla \cdot (\mu\nabla\vec{u}) + \vec{g} \tag{3.27}$$

$$\frac{DT}{Dt} = \alpha\nabla^2 T \tag{3.28}$$

$$\frac{DC}{Dt} = D\nabla^2 C \tag{3.29}$$

Equation 3.27 is simplified in a similar way to natural convection problem in Section 3.3. However, density is considered to be a function of both temperature and concentration, $\rho = \rho(T, C)$, while applying Boussinesq approximation in double diffusion problems. Accordingly, Taylor series expansion of density, ρ, around a reference density, ρ_0, includes terms associated with concentration C.

$$\rho = \rho_0 + \left(\frac{\partial \rho}{\partial T}\right)_P (T - T_0) + \left(\frac{\partial \rho}{\partial C}\right)_P (C - C_0) + \dots \tag{3.30}$$

Similarly, volumetric coefficient of solutal expansion is introduced.

$$\beta_S = -\frac{1}{\rho}\left(\frac{\partial \rho}{\partial C}\right)_P \tag{3.31}$$

In double diffusion problems, volumetric coefficient of thermal expansion is denoted by β_T. Then, density variation is simplified as.

$$\rho - \rho_0 = -\rho\left(\beta_T(T - T_0) + \beta_S(C - C_0)\right) \tag{3.32}$$

Inserting Equation 3.32 into Equation 3.10 and assuming gravity is in the negative y-direction, the following form of the momentum equation is obtained.

$$\frac{D\vec{u}}{Dt} = -\frac{1}{\rho}\nabla p + \frac{1}{\rho}\nabla \cdot (\mu \nabla \vec{u}) + g\left(\beta_T(T - T_0) + \beta_S(C - C_0)\right)\hat{j} \tag{3.33}$$

Finally, Equations 3.26, 3.27, 3.28 and 3.29 are non-dimensionalized using

$$(x^*, y^*) = \frac{(x, y)}{L} \tag{3.34}$$

$$\vec{u}^* = \vec{u}\frac{L}{\alpha} \tag{3.35}$$

$$t^* = t\frac{\alpha}{L^2} \tag{3.36}$$

$$T^* = \frac{T - T_C}{T_H - T_C} \tag{3.37}$$

$$C^* = \frac{C - C_C}{C_H - C_L} \tag{3.38}$$

$$
\begin{aligned}
p^* &= p\frac{L^2}{\rho_0 \alpha^2} && (3.39)\\
\rho^* &= \frac{\rho}{\rho_0} && (3.40)\\
Pr &= \frac{\nu}{\alpha} && (3.41)\\
Le &= \frac{\alpha}{D} && (3.42)\\
Ra_T &= \frac{g\beta_T \left(T_H - T_C\right) L^3}{\nu\, \alpha} && (3.43)\\
Ra_S &= \frac{g\beta_S \left(C_H - C_L\right) L^3}{\nu\, D} && (3.44)
\end{aligned}
$$

where L is a characteristic length, T_H is the maximum temperature, T_C is the minimum temperature, C_H is the high concentration, C_L is the low concentration, Pr is Prandtl number, Ra_T is thermal Rayleigh number, Ra_S is solutal Rayleigh number and Le is Lewis number. Then, the following non-dimensional form of governing equations are obtained.

$$
\begin{aligned}
&\nabla \cdot \vec{u}^* = 0 && (3.45)\\
&\frac{D\vec{u}^*}{Dt^*} = -\frac{1}{\rho^*}\nabla p^* + Pr\left(\frac{1}{\rho^*}\nabla\cdot(\rho^*\nabla\vec{u}^*)\right) \\
&\qquad + \left[PrRa_T(T^* - 0.5) + PrRa_S(C^* - 0.5)\right]\hat{j} && (3.46)\\
&\frac{DT^*}{Dt^*} = \nabla^2 T^* && (3.47)\\
&\frac{DC^*}{Dt^*} = \frac{1}{Le}\nabla^2 C^* && (3.48)
\end{aligned}
$$

Equations 3.45, 3.46, 3.47 and 3.48 are solved using the projection method described in Section 2.3

3.5. Two-phase Flows

Two-phase flow is one of the most challenging problems in Computational Fluid Dynamics (CFD). Modeling the interface and its evolution during the course of a simulation usually requires additional tools, equations and computations. Especially for grid-based methods, a significant amount of interpolations, calculations and operations are required, which result in a higher computational cost. On the other hand, SPH,

due to its meshless nature, is requires no additional models, equations or computations. Since SPH completely relies on discrete summations on particles that have an initially defined mass, interface is not need to be defined, modeled or explicitly tracked. The interface itself is automatically defined in SPH. This property makes SPH a very powerful tool in simulating two-phase and free surface flows.

In SPH, an initial color is assigned to each particle. If a particle i belongs to Fluid 1, its color is $C_i = 1$ and if it belongs to Fluid 2, its color is $C_i = 0$. Accordingly, density and dynamic viscosity of a particle i is calculated as

$$\overline{\rho}_i = \rho_2 + (\rho_1 - \rho_2) C_i \tag{3.49}$$

$$\overline{\mu}_i = \mu_2 + (\mu_1 - \mu_2) C_i \tag{3.50}$$

However, discontinuities existing in the computational domain are usually avoided. In case of two-phase flows, density and viscosity fields are discontinuous around the interface. Thus, variables such as density and viscosity are smoothed out across the interface.

$$\rho_i = \sum_j V_j \overline{\rho}_j W_{ij} \tag{3.51}$$

$$\mu_i = \sum_j V_j \overline{\mu}_j W_{ij} \tag{3.52}$$

where $V_j = \left(\sum_j W_{ij}\right)^{-1}$ is the volume of particle j. Since density is calculated in a similar way in SPH, Equations 3.51 and 3.52 can be applied for all particles. After obtaining continuous density and viscosity fields, SPH simulations are carried out as in single-phase flows.

In this thesis, two-phase flow is investigated in terms of topological changes of interfaces and Rayleigh-Taylor instability. Four different problems such as rising bubble, droplet fall, bursting bubble at the free surface and droplet fall onto the free surface are studied for topological changes. On the other hand, Rayleigh-Taylor instability is

simulated as a two-phase flow instability problem. Furthermore, SPH results are compared to Level Set method. For this reason, surface tension models are not employed during the simulations.

3.5.1. Topological Changes of Interfaces

A difficult task while simulating two-phase flow is to capture topological changes such as merging and pinching off. In case of merging, two or more interfaces are transformed into a single interface. On the other hand, in case of pinching off, two or more interfaces are formed from a single interface. Test problems such as rising bubble, droplet fall, bursting bubble at the free surface and droplet fall onto the free surface are considered for studying topological changes as seen in Figure 3.7. SPH is tested in these four different problems. Moreover, results are compared to results obtained from Level Set method.

In all of four problems, Fluid 1 is the heavier and more viscous fluid compared to Fluid 2. Density ratio is $\rho_1/\rho_2 = 1000$ and viscosity ratio is $\mu_1/\mu_2 = 100$. In rising bubble problem, a bubble of radius, $R = 0.125$, is released in an environment where surrounding is the heavier fluid as drawn in Figure 3.7(a). Center of the bubble is located at $(x_c, y_c) = (0, -0.3)$ and Reynolds number is $Re = 1000$. As bubble rises, shape change of bubble is monitored. In other words, evolution of interface is tracked. In term of topological changes, pinching off is also observed. Furthermore, in droplet fall problem, a droplet of radius, $R = 0.125$, is released in a environment where surrounding is the lighter fluid as depicted in Figure 3.7(b). Center of the bubble is located at $(x_c, y_c) = (0, 0.3)$ and Reynolds number is $Re = 1000$. As it falls, droplet does not exhibit a significant deformation. However, when the droplet hits the ground, it spreads out dramatically.

In bursting bubble problem, a bubble is released just below a free surface separating the heavier and lighter fluid as seen in Figure 3.7(c). The bubble is located at $(x_c, y_c) = (0, -0.35)$, free surface is on the line $y_s = -0.2$ and Reynolds number is $Re = 1000$. After bubble is released, it merges with free surface. Moreover, in droplet

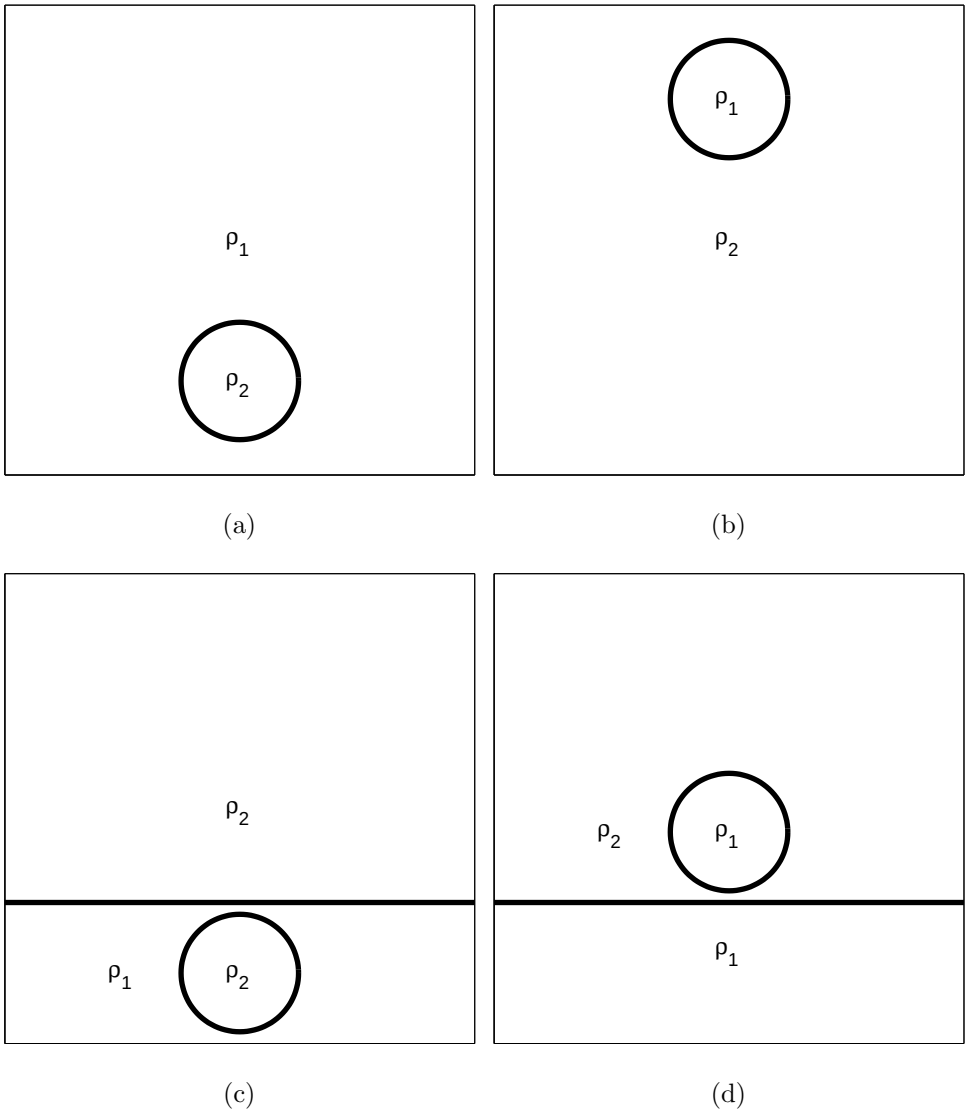

Figure 3.7. (a) Rising bubble, (b) Droplet fall, (c) Bursting bubble at the free surface, (d) Droplet fall onto the free surface.

fall problem, a droplet is released just above a free surface separating the heavier and lighter fluid as shown in Figure 3.7(d). The droplet is located at $(x_c, y_c) = (0, -0.05)$, free surface is located at $y_s = -0.2$ and Reynold number is set $Ra = 1000$. After the droplet is released, it meets the free surface and merging occurs.

3.5.2. Rayleigh-Taylor Instability

In Rayleigh-Taylor instability, a heavier fluid is placed onto a lighter fluid as shown in Figure 3.8. Density ratio is $\rho_1/\rho_2 = 2$, viscosity ratio is $\mu_1/\mu_2 = 1$ and

Reynolds number is $Re = 400$. Furthermore, an initial disturbance on the interface is defined by a sinusoidal function

$$Y = 0.15sin(2\pi x) - 0.5 \tag{3.53}$$

After two fluids are released, the heavy fluid tries to flow downward and the light fluid tries to flow upward in a certain fashion. This depends on density ratio ρ_1/ρ_2, viscosity ratio μ_1/μ_2, Reynolds number Re and initial disturbance.

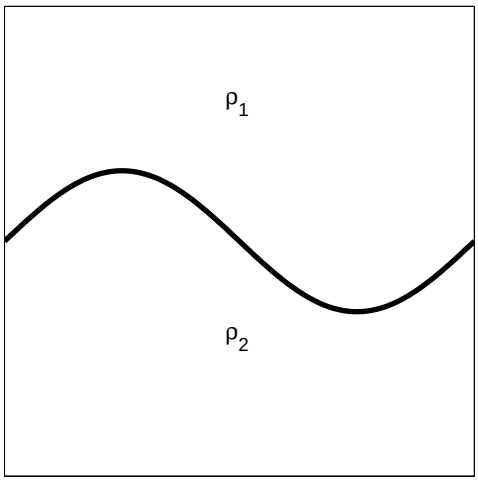

Figure 3.8. Rayleigh-Taylor Instability.

4. RESULTS AND DISCUSSION

In this study, convective-diffusive transport is studied by Incompressible SPH (ISPH) technique with particle shifting method due to Xu [13]. Mirror particle method proposed by Morris *et al.* is implemented for boundary particle modeling. Using the ISPH code developed during the thesis study, isothermal, non-isothermal, double-diffusive and two-phase flows are simulated as described in Chapter 3.

4.1. Lid-Driven Cavity

Lid-driven cavity problem is simulated for Reynolds number $Re = 100$, 400, and 1000 by 3600 particles. At the beginning, particles are located at uniform grid points such that initial particle spacing is $dx = 1/59$. Problem geometry and governing equations are discussed in Section 3.1.

In Figures 4.1, 4.2 and 4.3, result of lid-driven cavity problem is presented at $Re = 100$, 400, and 1000 respectively. Moreover, they are compared to results of Xu *et al.* [13]. It is shown that ISPH code developed during this thesis study is in a good agreement with results obtained in [13].

4.2. Vortex Spin-Down

Vortex spin-down problem is simulated for Reynolds number $Re = 10$, 100, and 1000 by 3600 particles. At the beginning, particles are located at uniform grid points such that initial particle spacing is $dx = 1/59$. Problem geometry and governing equations are discussed in Section 3.2

In Figures 4.4, 4.5 and 4.6, result of vortex spin-down problem is presented at $Re = 10$, 100, and 1000, respectively. Similar to the previous case, results obtain for vortex spin-down problem are compared to results of Xu *et al.* [13] and a good agreement is observed.

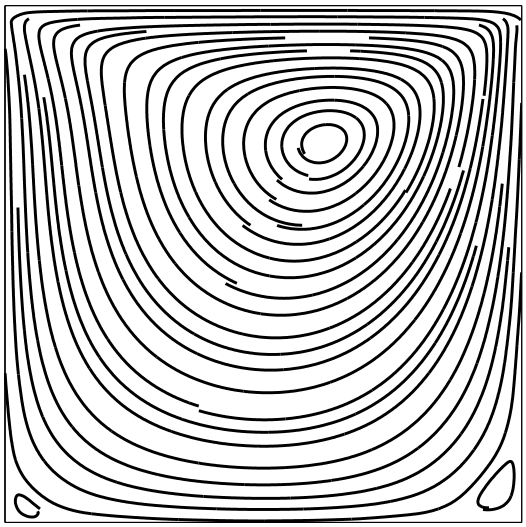

(a)

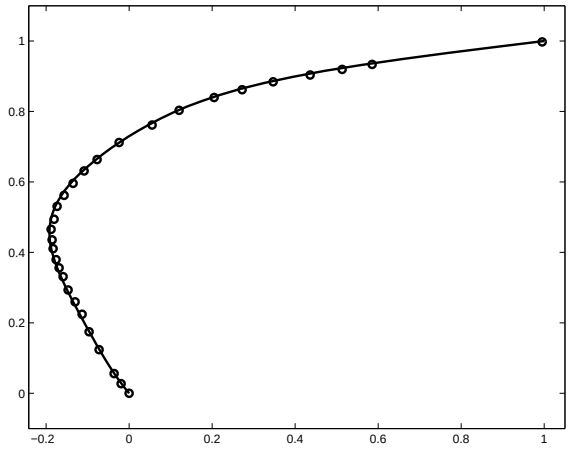

(b)

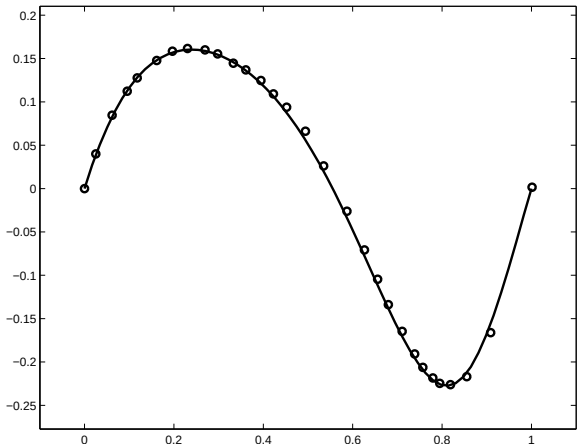

(c)

Figure 4.1. (a) Streamlines, (b) u-velocity and (c) v-velocity profiles for lid-driven cavity problem at $Re = 100$. — = Present ISPH code; **O** = ISPH code by Xu *et al.* [13] with 81×81 resolution.

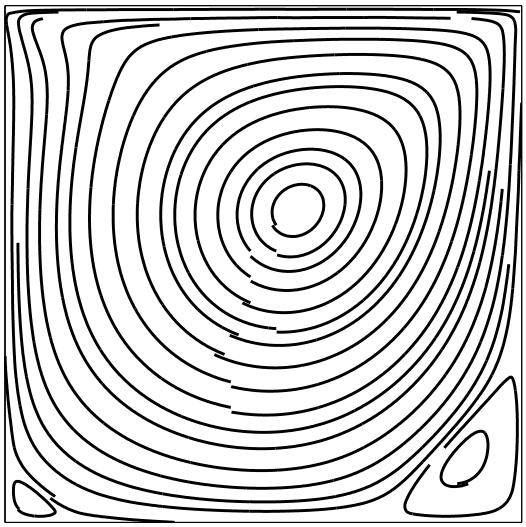

(a)

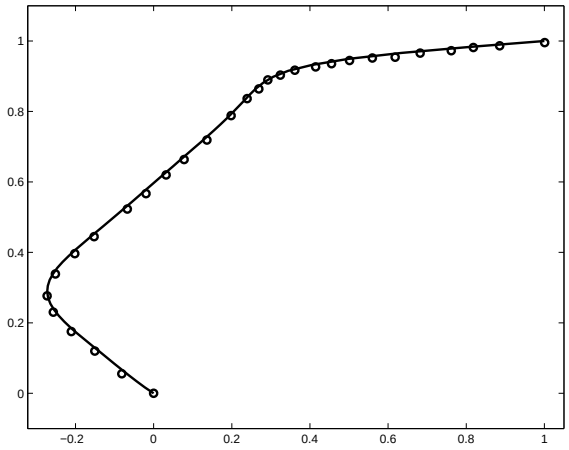

(b)

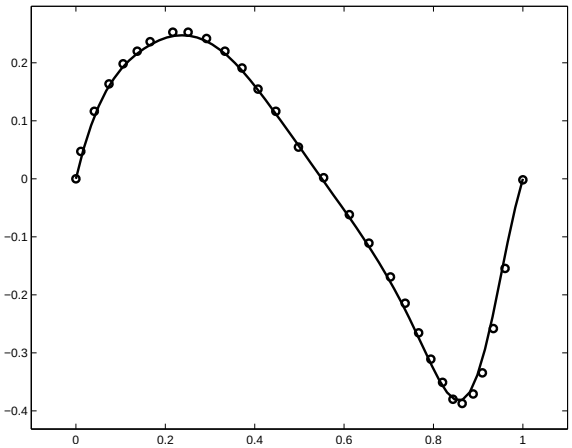

(c)

Figure 4.2. (a) Streamlines, (b) u-velocity and (c) v-velocity profiles for lid-driven cavity problem at $Re = 400$. — = Present ISPH code; **O** = ISPH code by Xu *et al.* [13] with 81×81 resolution.

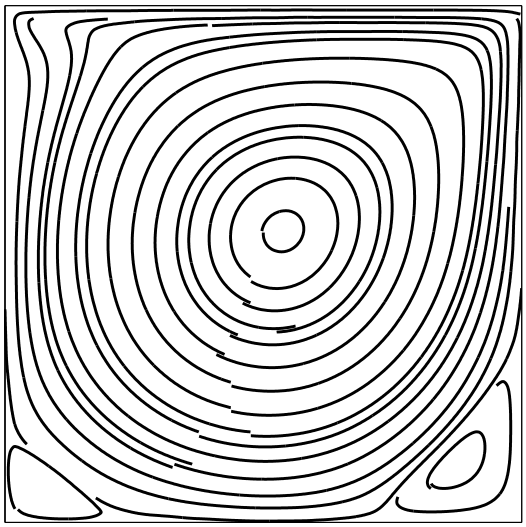

(a)

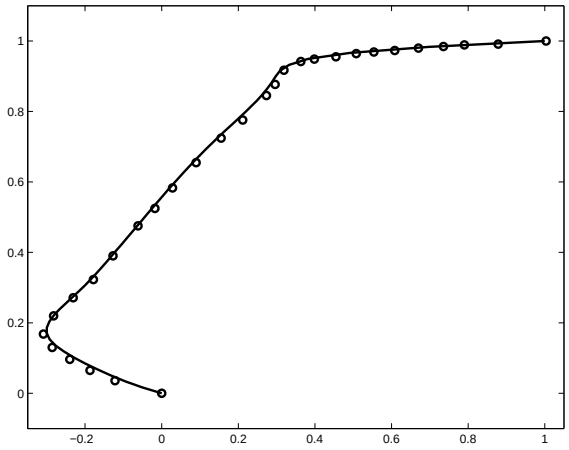

(b)

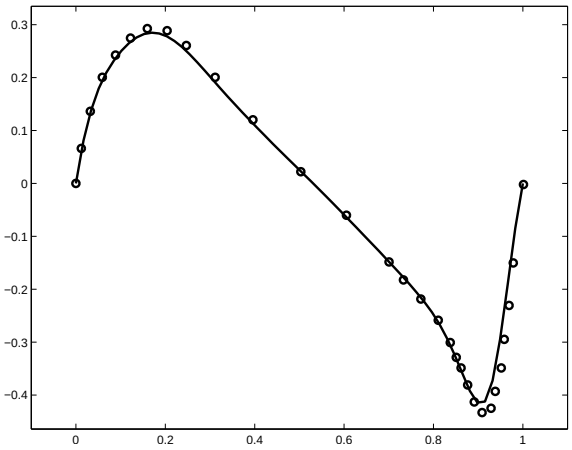

(c)

Figure 4.3. (a) Streamlines, (b) u-velocity and (c) v-velocity profiles for lid-driven cavity problem at $Re = 1000$. — = Present ISPH code; **O** = ISPH code by Xu *et al.* [13] with 81×81 resolution.

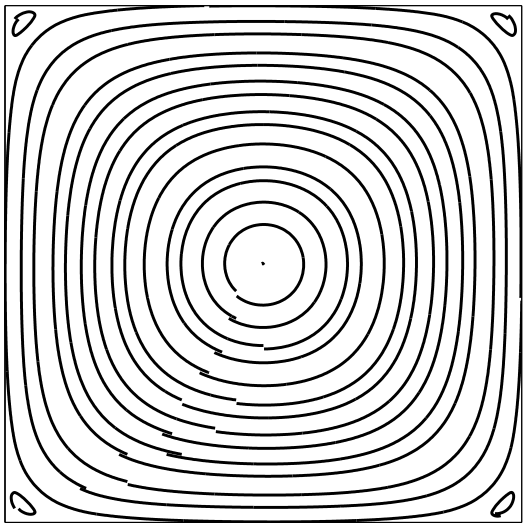

(a)

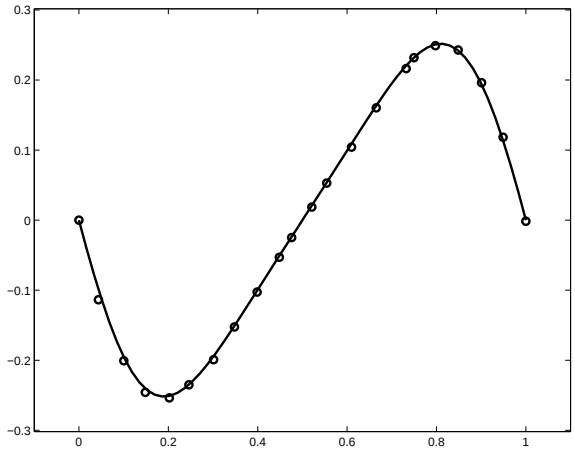

(b)

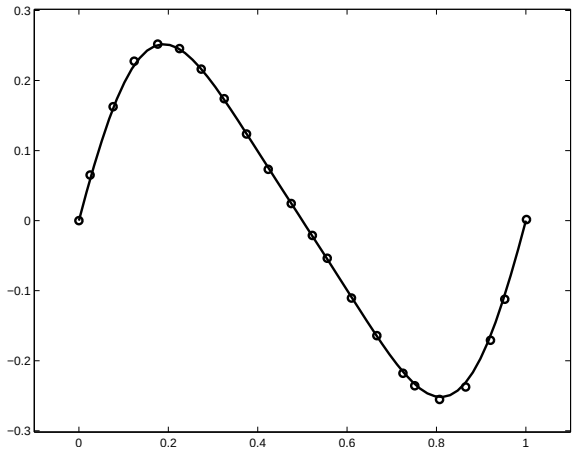

(c)

Figure 4.4. (a) Streamlines, (b) u-velocity and (c) v-velocity profiles for vortex spin-down problem at $Re = 10$. — = Present ISPH code; **O** = ISPH code by Xu *et al.* [13] with 41×41 resolution.

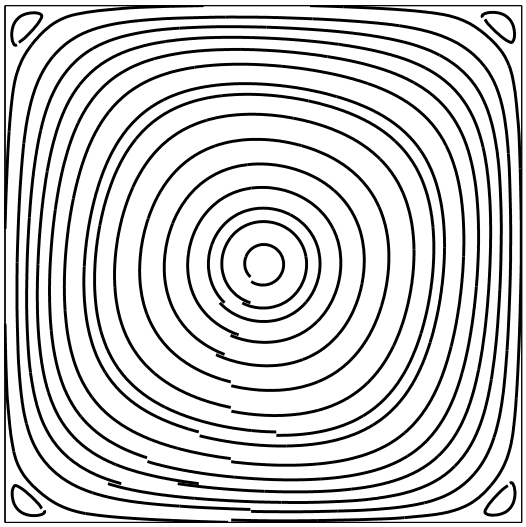

(a)

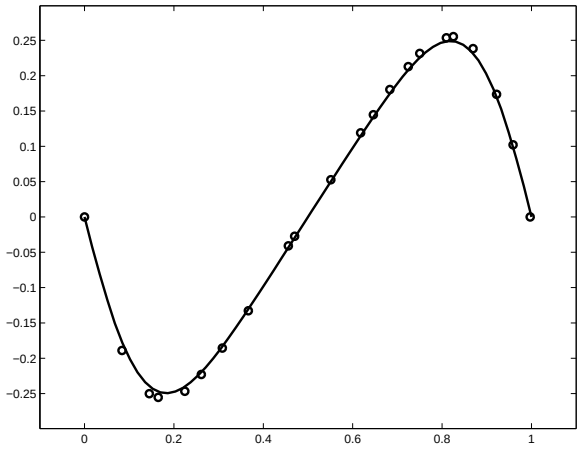

(b)

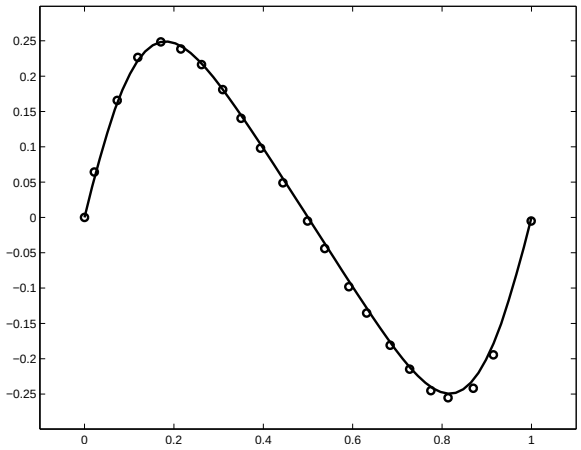

(c)

Figure 4.5. (a) Streamlines, (b) u-velocity and (c) v-velocity profiles for vortex spin-down problem at $Re = 100$. — = Present ISPH code; **O** = ISPH code by Xu *et al.* [13] with 41×41 resolution.

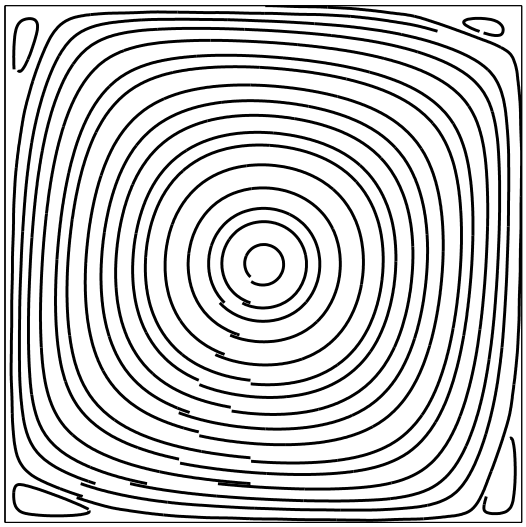

(a)

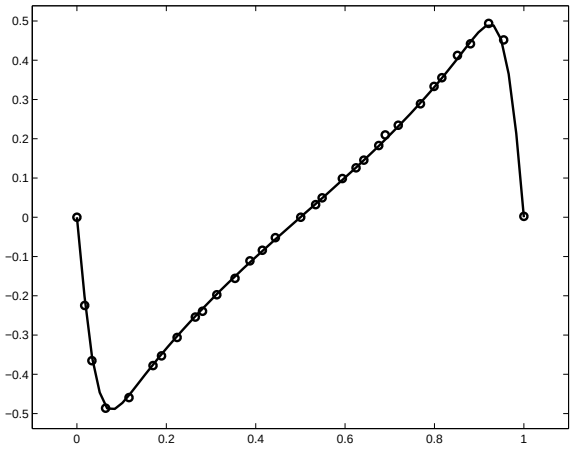

(b)

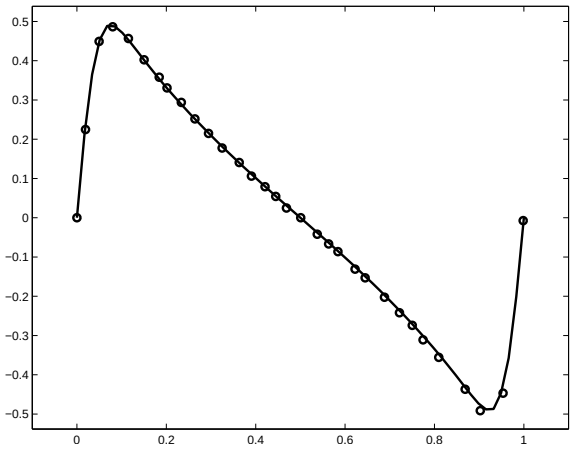

(c)

Figure 4.6. (a) Streamlines, (b) u-velocity and (c) v-velocity profiles for vortex spin-down problem at $Re = 1000$. — = Present ISPH code; **O** = ISPH code by Xu *et al.* [13] with 41×41 resolution.

4.3. Natural Convection

Despite its significance, natural convection has not been studied by ISPH technique in detail. In this thesis, a comprehensive analysis of natural convection using ISPH technique is provided. Natural convection is investigated under three different problems. First problem is natural convection in a square cavity problem in which effect of Rayleigh number Ra is investigated. In this case, grid-based ISPH method is used to simulate the flow and results obtained is compared to available results in the literature. It is seen that there exists a good agreement between the results obtained by the proposed technique and literature. Since particle disorder is not seen in grid-based ISPH, it is thought to be an upper limit for SPH computations. Grid-based ISPH technique is only implemented in the first case. Second problem is Rayleigh-Bénard convection, in which multiple states of the solutions are shown. Different solutions are obtained for different velocity initial conditions. In the last problem, natural convection at the onset of instability is discussed. It is shown that regardless of the initial conditions, flow field shows oscillatory multicellular structures for aspect ratios $AR > 1$.

4.3.1. Natural Convection in a Square Cavity

Effect of Rayleigh number on the flow field is investigated on 81×81 grids. In Figure 4.7, streamlines and temperature contours are presented for Ra numbers between 10^3 and 10^6. For low Ra numbers, streamlines include only one primary vortex. As Ra number increases, especially for $Ra = 10^5$, secondary vortices occur toward the upper-left and lower-right corners. For high Ra numbers, especially for $Ra = 10^6$, secondary vortices near the upper-left and lower-right hand corners approach to left and right walls respectively and an additional secondary vortex appears in the middle of the cavity. Velocity values near the walls are higher compared to velocity values in the near neighborhood of the center of the cavity.

Moreover, temperature contours are almost vertical for low Ra number simulations. For $Ra = 10^3$, temperature decreases almost linearly in positive x-direction. As Ra number increases, temperature contours becomes more and more horizontal. For

instance, temperature contours are almost horizontal in the central region of the cavity for $Ra = 10^6$. This can be seen also in Figure 4.8.

Furthermore, in Figure 4.8, it can be observed that maximum velocities exist near the walls and minimum velocities exist in the middle region of the cavity. Since left and right walls are the locations of global maxima and minima for temperature, location of peaks in v-velocity profile must be closer to walls than the location of peaks in u-velocity profile, which is also observed in Figure 4.8.

Results obtained in this study are compared to the results available in literature. In Table 4.1, mean Nusselt number (Nu_m), maximum Nusselt number (Nu_{max}), minimum Nusselt number, (Nu_{min}), maximum u velocity (u_{max}), maximum v velocity (v_{max}) for Rayleigh number interval $10^3 - 10^6$ are compared. Nusselt number values calculated at the hot wall, u velocity values are calculated at the half width plane of the cavity and v velocity values are calculated at the half height plane of the cavity. Locations of maximum and minimum points in Table 4.1 are chosen to be the actual location of grid points. In other words, no interpolation is made to find the maximum and minimum points. Results show that original solution obtained in this study is in a very good agreement with available results in literature.

4.3.2. Rayleigh-Bénard Convection

In this case, boundary conditions are changed. Neumann boundary condition for temperature is applied at the vertical walls and constant temperatures T_H and T_C are applied at the horizontal walls. Initially, temperature varies linearly from the hot wall to the cold. Therefore, boundary and initial conditions are symmetric with respect to mid-width plane of the cavity. As a consequence, ISPH does not lead to a solution if all particles are initially stationary. For example, all particles near the hot wall tend to move upward while all particles near the cold wall tend to move downward. After a certain time step depending on Ra, particles are clustered in the middle region of the cavity, incompressibility is broken down and solution blows up. Therefore, it is a necessity that an initial disturbance must be introduced into the flow field. In this

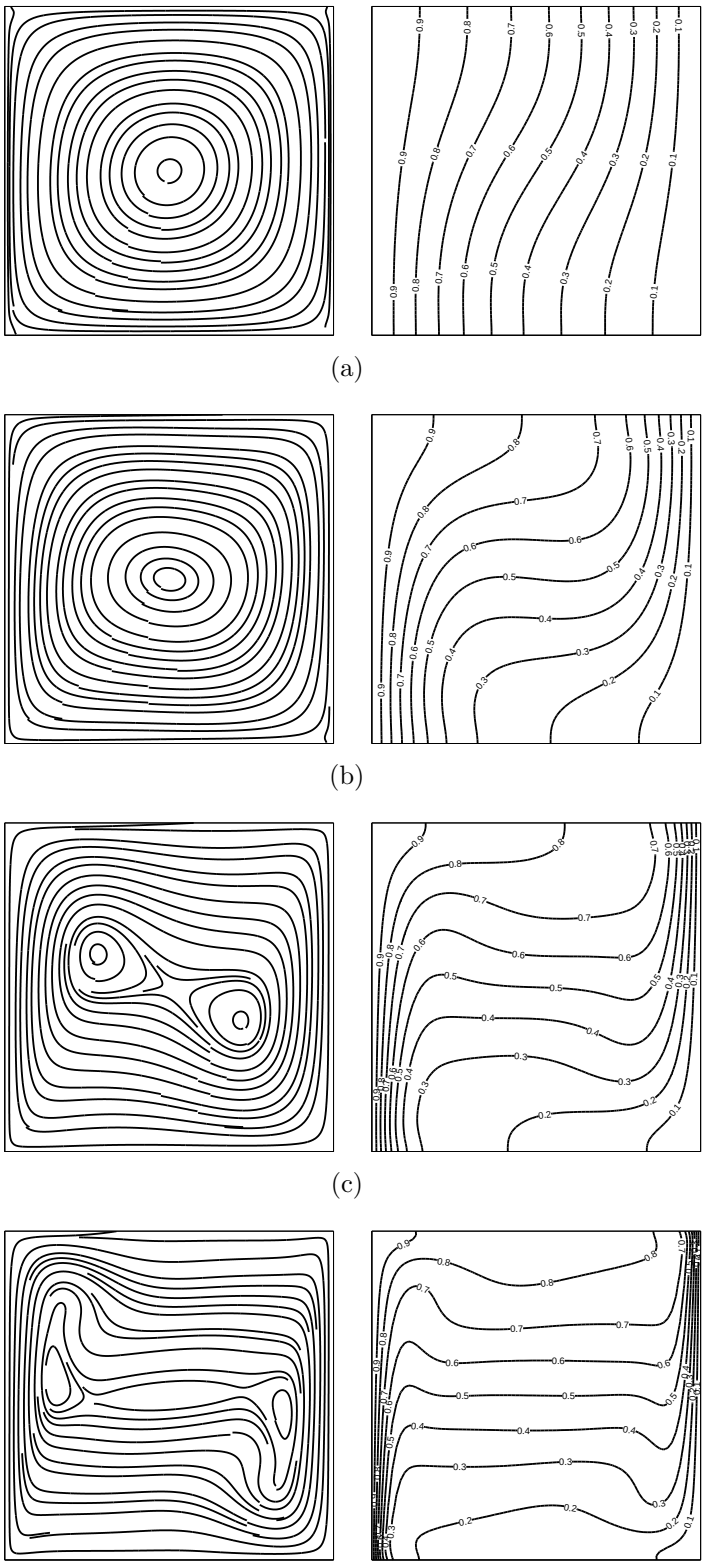

Figure 4.7. Streamlines and temperature profiles at (a)$Ra = 10^3$, (b)$Ra = 10^4$, (c)$Ra = 10^5$ and (d)$Ra = 10^6$.

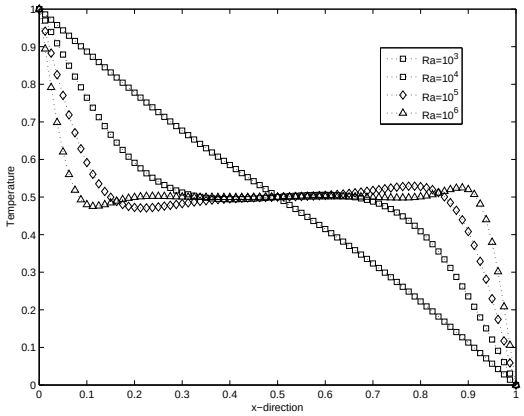

(a)

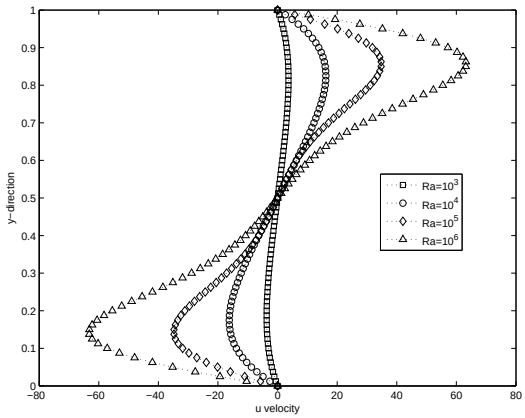

(b)

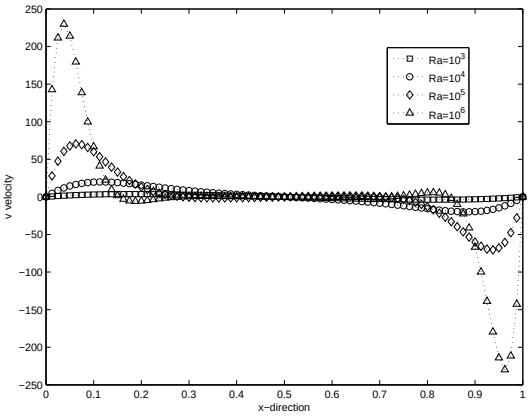

(c)

Figure 4.8. (a)Temperature profiles in x-direction at half width, (b) Velocity profiles in x-direction at half width and (c) Velocity profiles in y-direction at half height from $Ra = 10^3$ to $Ra = 10^6$.

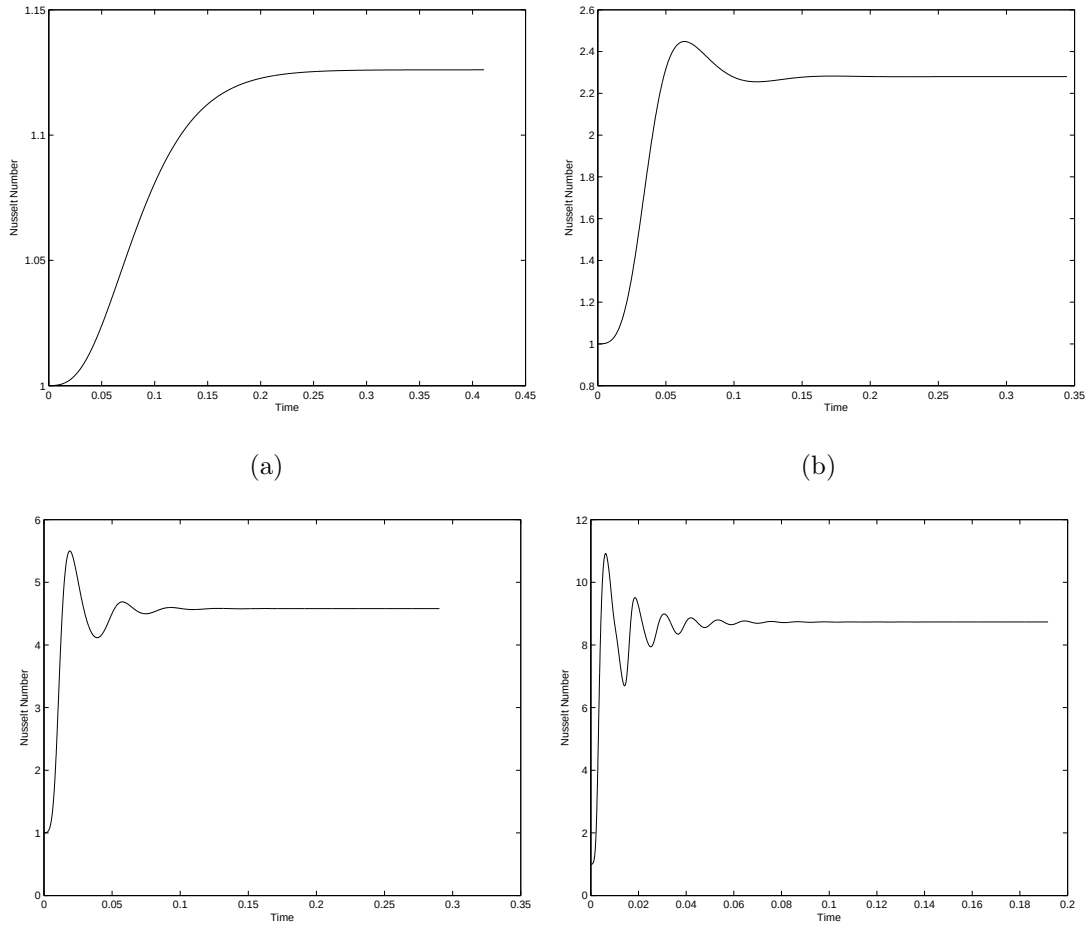

(a) (b)

(c) (d)

Figure 4.9. Nu_m values on the hot wall for (a) $Ra = 10^3$ (b)$Ra = 10^2$ (c)$Ra = 10^5$ (d) $Ra = 10^6$.

Table 4.1. Comparison of Nu_m, Nu_{max}, Nu_{min}, u_{max} and v_{max} Data with Literature.

	Present Work	de Vahl Davis [36]	Barakos *et al.* [37]	Wakashima and Saitoh [38]	Fusegi *et al.* [39]
			$Ra = 10^3$		
Nu_m	1.1192	1.116	1.114	-	1.104
$Nu_{max}(y/L)$	1.5109(0.0875)	1.501(0.087)	1.581(0.099)	-	1.420(0.083)
$Nu_{min}(y/L)$	0.689(1.000)	0.694(1.000)	0.67(0.994)	-	0.764(1.000)
$u_{max}(y/L)$	3.6662(0.8125)	3.634(0.813)	4.0768(0.806)	-	3.5172(0.833)
$v_{max}(x/L)$	3.7203(0.175)	3.679(0.179)	4.1301(0.181)	-	3.4906(0.200)
			$Ra = 10^4$		
Nu_m	2.2566	2.234	2.245	2.0676	2.302
$Nu_{max}(y/L)$	3.5432(0.1375)	3.545(0.149)	3.539(0.143)	-	3.652(0.623)
$Nu_{min}(y/L)$	0.5844(1.000)	0.592(1.000)	0.583(9.994)	-	0.611(1.000)
$u_{max}(y/L)$	16.2066(0.8250)	16.182(0.823)	16.2625(9.818)	16.7259(0.8250)	16.9366(0.817)
$v_{max}(x/L)$	19.8964(0.1125)	19.509(0.120)	19.7172(0.119)	18.6892(0.1125)	18.9588(0.117)
			$Ra = 10^5$		
Nu_m	4.5260	4.51	4.51	4.3907	4.646
$Nu_{max}(y/L)$	7.5841(0.0875)	7.761(0.085)	7.636(0.085)	-	7.795(0.083)
$Nu_{min}(y/L)$	0.7429(1.000)	0.736(1.000)	0.733(0.999)	-	0.787(1.000)
$u_{max}(y/L)$	34.7451(0.8625)	34.81(0.855)	35.1725(0.859)	37.7838(0.8500)	39.1694(0.855)
$v_{max}(x/L)$	70.4475(0.0625)	68.22(0.066)	69.7462(0.066)	65.2823(0.0625)	65.8152(0.065)
			$Ra = 10^6$		
Nu_m	8.6123	8.798	8.806	8.8681	9.012
$Nu_{max}(y/L)$	16.1274(0.0375)	18.076(0.0456)	17.442(0.0368)	-	17.670(0.0379)
$Nu_{min}(y/L)$	1.0823(1.000)	1.005(1.000)	1.001(0.999)	-	1.257(1.000)
$u_{max}(y/L)$	63.0338(0.8625)	65.33(0.851)	64.8814(0.859)	68.2939(0.8500)	70.7797(0.856)
$v_{max}(x/L)$	229.7988(0.0375)	216.75(0.0387)	220.7651(0.039)	219.5855(0.0375)	218.2373(0.033)

thesis, a non-zero velocity field is defined initially in order to create this disturbance. Moreover, different initial conditions are considered and expectedly, multiple solutions are obtained for the same problem.

In Figure 4.10, streamlines and temperature field at $Ra = 15000$ is plotted. In Figure 4.10(a) and Figure 4.10(b), initial velocity fields are given as

$$u = -50\, sin(\pi\, x) cos(\pi\, y) \tag{4.1}$$

$$v = 50\, cos(\pi\, x) sin(\pi\, y) \tag{4.2}$$

and

$$u = 50\, sin(\pi\, x) cos(\pi\, y) \tag{4.3}$$

$$v = -50\, cos(\pi\, x) sin(\pi\, y) \tag{4.4}$$

respectively. It is observed that different initial velocity fields lead to different solutions which means that this problem does not have a unique solution and both solutions satisfy Momentum and Energy equations.

Similarly, in Figure 4.10(c) and Figure 4.10(d), initial velocity fields are given as

$$u = -50\, sin(\pi\, x) cos(2\pi\, y) \tag{4.5}$$

$$v = 50\, cos(\pi\, x) sin(2\pi\, y) \tag{4.6}$$

and

$$u = 50\, sin(\pi\, x) cos(2\pi\, y) \tag{4.7}$$

$$v = -50\, cos(\pi\, x) sin(2\pi\, y) \tag{4.8}$$

Although the previous solutions $S1^{\pm}$ are more probable ones, ISPH code is able to capture 2-cell streamline structures $S2^{\pm}$. Moreover, solutions $S2^{\pm}$ are stable.

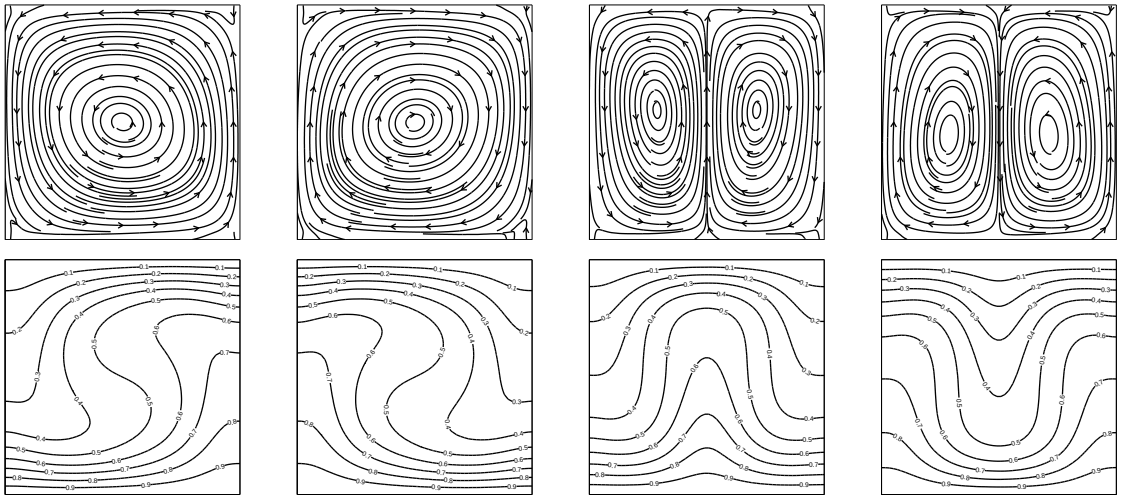

(a) (b) (c) (d)

Figure 4.10. Multiple States of Solutions $S1^{\pm}$ and $S2^{\pm}$ at $Ra = 15000$.

4.3.3. Natural Convection at the onset of Instability

CASE I:*Aspect Ratio AR = 1*

In the first case of the simulations, natural convection in a cavity is simulated where aspect ratio is $AR = 1$. A linear initial temperature field is set at the side walls while the bottom and top walls are remained at constant hot and cold temperatures, respectively. Initial velocity field is given as

$$u = 30sin(\pi\, x)cos(\pi\, y) \tag{4.9}$$

$$v = -30cos(\pi\, x)sin(\pi\, y) \tag{4.10}$$

Therefore, boundary and initial conditions are symmetric with respect to vertical axis. In Figure 4.11, streamlines, temperature field and time history of mean Nusselt number, Nu_m, at top and bottom walls is plotted. It is seen that both streamlines and temperature field are remained symmetric with respect to vertical axis and mean Nusselt numbers reach steady state. It is worth noting that mean Nusselt number

values are not equal at top and bottom walls.

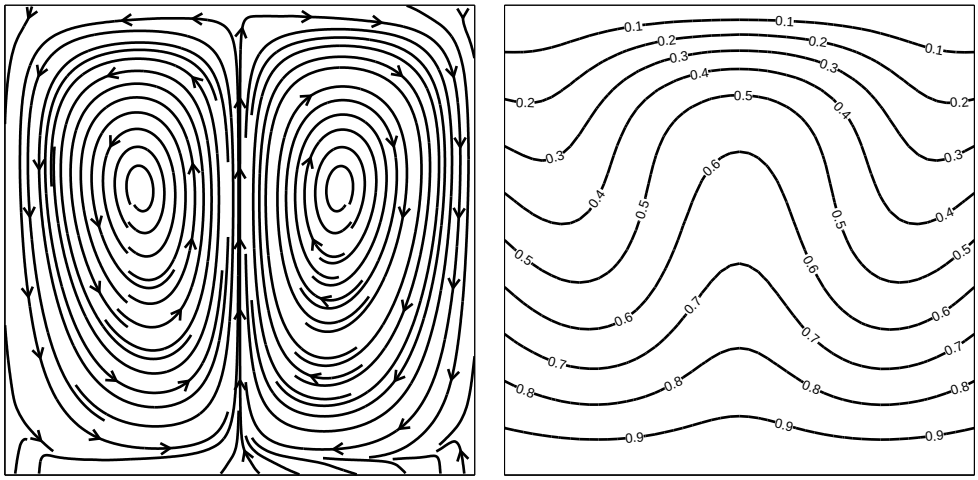

(a) (b)

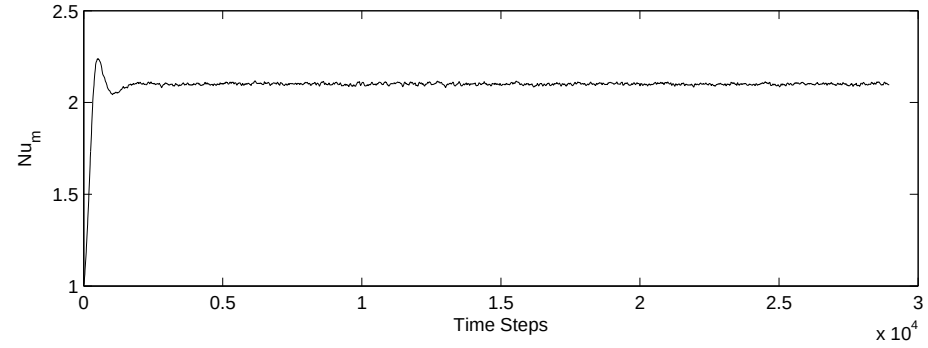

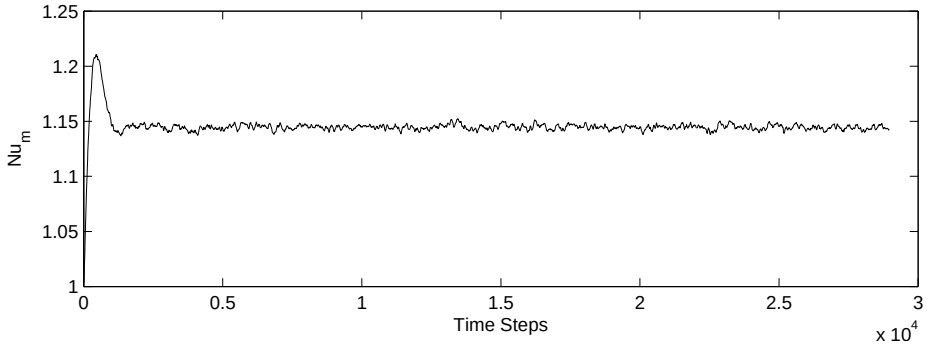

(c)

Figure 4.11. (a) Streamlines, (b) Temperature, (c) Nu_m at top and bottom walls for $Ra = 15000$ and $AR = 1$.

CASE II:*Aspect Ratio AR = 1.5*

In the second case of the simulations, aspect ratio is increased to $AR = 1.5$. As in the first case, a linear temperature variation at the side walls is set while the

bottom and top walls are kept at constant hot and cold temperatures. In order to have symmetric streamlines with respect to vertical axis at beginning of the simulations, velocity field is set to be

$$u = 30sin\left(0.5\pi\left(x+1\right)\right)cos\left(2\pi\left(y+0.5\right)\right) \quad (4.11)$$

$$v = -30cos\left(0.5\pi\left(x+1\right)\right)sin\left(2\pi\left(y+0.5\right)\right) \quad (4.12)$$

Similar to the previous case, all initial and boundary conditions are symmetric with respect to the vertical axis. However, behavior of flow in Case II does not resemble Case I. The solution is not symmetric despite the symmetry in initial and boundary conditions. In addition, a constant steady state is not reached. In fact, flow field is observed to be oscillatory in Case II. This oscillatory behavior of flow is presented in Figure 4.12 and Figure 4.13.

In Figure 4.12, time history of Nu_m at the bottom and top walls is depicted. It is seen that Nu_m values do not reach to a constant steady state value but they show oscillations around a mean value. After flow is initiated, Nu_m at the top wall sharply increases to its global maximum. Then, it goes through a sudden decrease to a point where it becomes more or less steady. On the other hand, Nu_m at the bottom wall does not exhibits rapid increase and decrease as Nu_m at the top wall but it reaches a point after which its value is almost constant. However, this steadiness is distorted and flow field enters a periodic interval.

In the periodic interval, the evolution of Nu_m is marked with seven vertical lines that corresponds to characteristics of the solution. Accordingly, in Figure 4.13, cellular structures in streamlines and temperature contours are drawn at these instances. At Line 1, periodicity of the solution begins. Moreover, Nu_m at the bottom wall is at its minimum at Line 1. Velocity field consists of two cells, one being a primary cell and the

other being a secondary cell at the upper right-hand corner. As time goes on toward Line 2, value of Nu_m at both the bottom and the top walls increases and it reaches its maximum for Nu_m at the bottom wall. This increase results in two secondary cells at the corners. Line 3 is drawn at an intermediate time step where Nu_m at both the bottom and upper walls declines. During this decrease, primary cell is divided into two cells. Moreover, secondary cell in the upper right-hand corner grows and becomes a primary cell while secondary cell in the lower left-hand corner shrinks. At Line 4, Nu_m at the bottom wall reaches its minimum, the first primary cells disappears and the second primary cell becomes the only primary cell in the flow field. Furthermore, secondary cell in the lower left-hand corner disappears and secondary cell in the upper left-hand corner becomes the only secondary cell remaining. Most important of all, this is the time step that corresponds to a half period, not a complete period. Although Nu values taken at Line 1 and 4 are the same, different velocity and temperature fields are observed at Line 1 and 4. Actually, these fields are mirror images of each other with respect to the vertical axis. Due to this symmetry of temperature fields at Line 1 and 2 with respect to the vertical axis, Nu_m values are the same since Nu_m on horizontal walls depends on temperature gradients in vertical axis and integration of temperature gradients along horizontal axis. In the second half period, flow develops in a similar fashion and completes its period at the Line 7. This can be seen by examining Figure 4.12 and the locations of the secondary cells at Lines 1, 4 and 7.

CASE III:*Aspect Ratio* $AR = 2$

In the last case of the simulations, aspect ratio is increased to $AR = 2$. Similar to previous cases, temperature varies linearly at the side walls and constant hot and cold temperatures are defined at the bottom and cold walls, respectively. In order to obtain a symmetric velocity field with respect to vertical axis at the beginning of the simulation, Equations 4.11 and 4.12 are used as the initial velocity field. Despite the symmetry in initial and boundary conditions with respect to the vertical axis, the solution is not symmetric and it exhibits oscillations as in Case II.

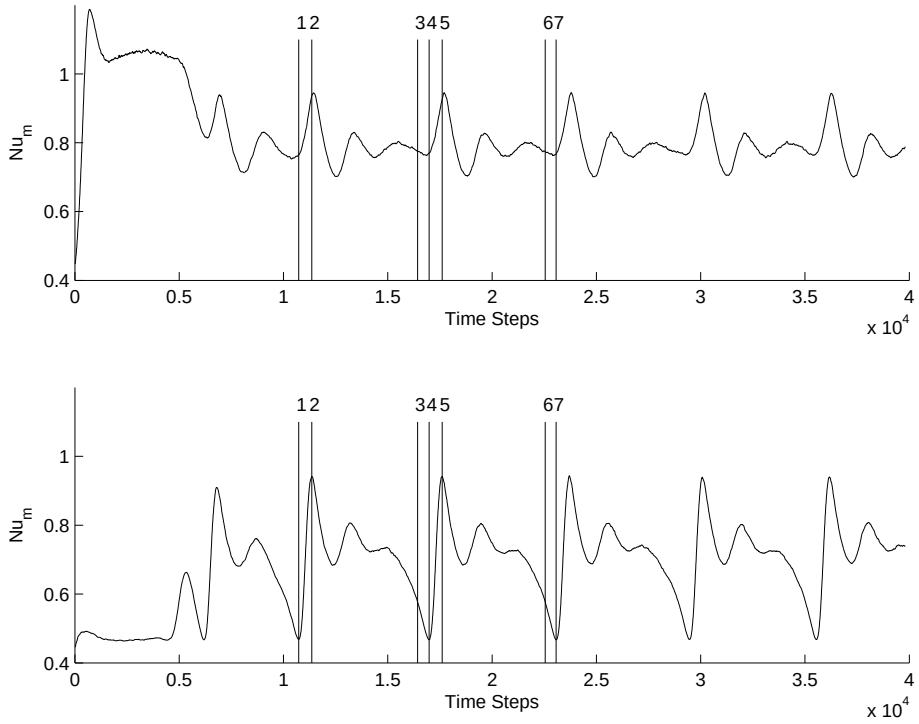

Figure 4.12. Nu_m at top and bottom walls at $Ra = 15000$ and $AR = 1.5$.

In Figure 4.14, Nu_m evolves in a fashion similar to Case II before it reaches the oscillatory interval. It is observed that Nu_m at the top wall passes through a sudden increase and a subsequent decrease to a point after which flow is more or less steady. Afterward, the steadiness ends and oscillations in flow field begins.

As in Case II, time history of Nu_m is marked with five vertical lines corresponding to characteristics of the solutions in Figure 4.14 and at these instances, streamlines and temperature contours are drawn in Figure 4.15. At Line 1, where periodicity starts, Nu_m at the bottom wall is at its maximum (in the periodic interval). Two primary cells and two secondary cells coexist. Lower primary cell is bigger than upper primary cell. At Line 2, Nu_m at the top wall is at its maximum. At this instance, upper primary cell is the bigger one. At Line 3, one period of oscillations is completed, which can be observed by examining Figure 4.15.

Although both solutions obtained in Case II and Case III are oscillatory, behavior of these oscillations differs. For instance, oscillations of Nu_m in Case III resembles a sinusoidal function while oscillations of Nu_m in Case II does not.

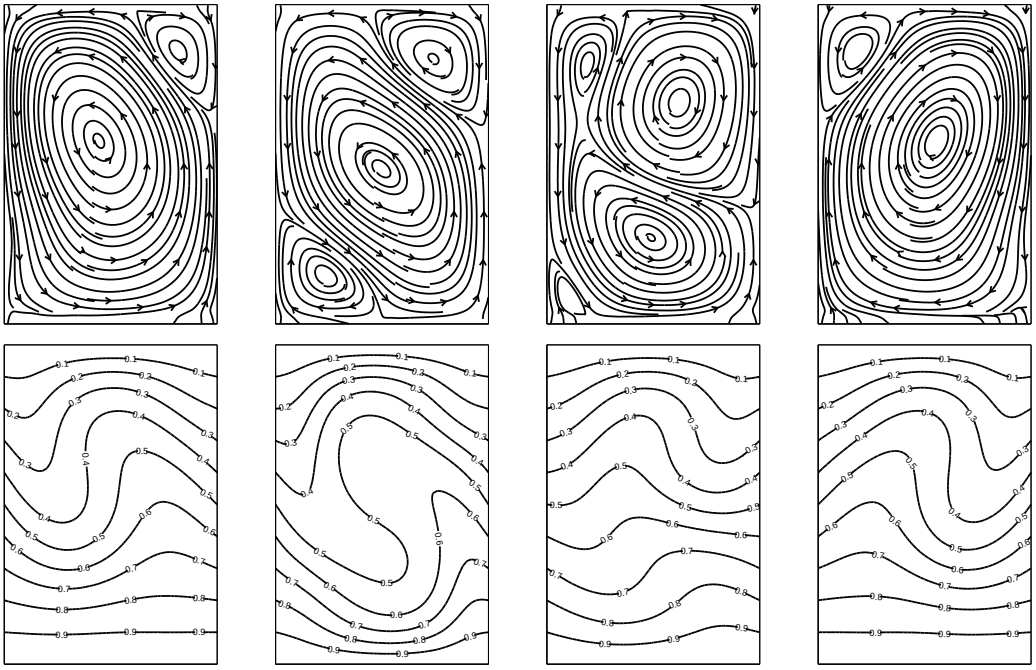

(a) ts=10730 (b) ts=11360 (c) ts=16430 (d) ts=16980

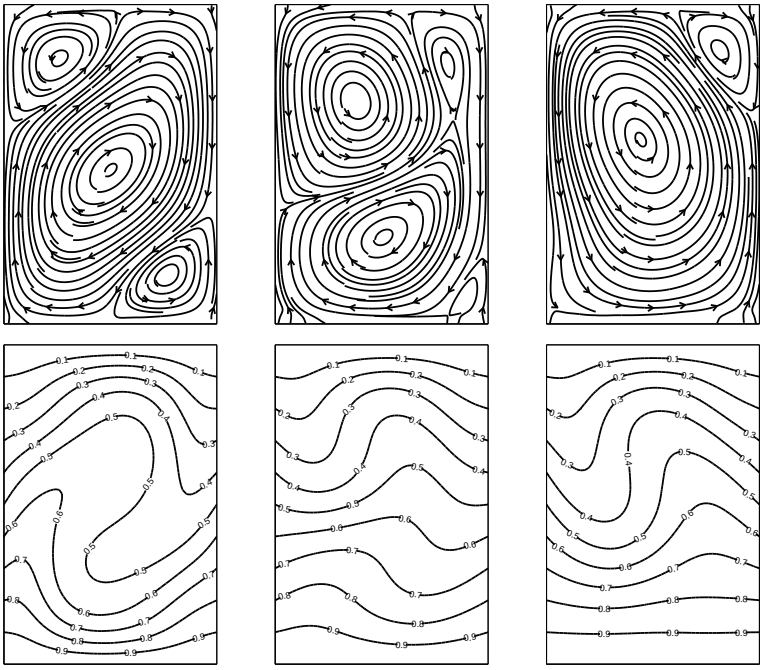

(e) ts=17610 (f) ts=22500 (g) ts=23070

Figure 4.13. Streamlines and Temperatures at Different Time Steps.

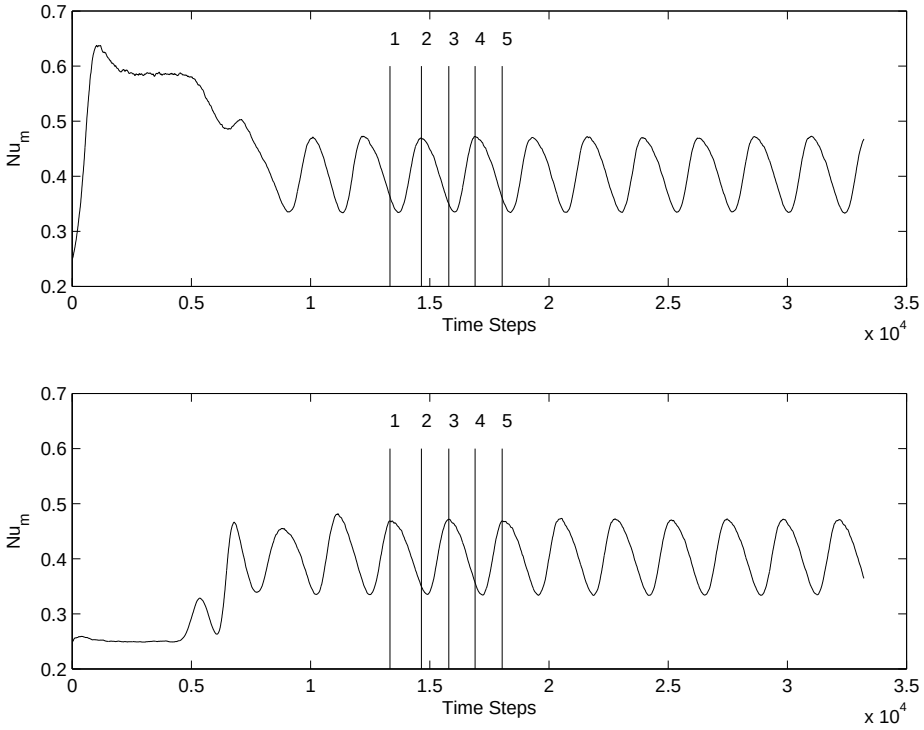

Figure 4.14. Nu_m at top and bottom walls at $Ra = 15000$ and $AR = 2$.

4.4. Double-Diffusion Problem

In pure natural convection problems, flow is generated by applying a temperature gradient. Similarly, in mass transfer problems, flow is generated by applying a concentration gradient. In double diffusion problems, flow is driven by applying both temperature and concentration gradient together. In other words, both heat and mass transfer result in fluid motion. These two mechanisms that drive flow may aid or oppose each other. For instance, if heat and mass transfer occur in the same direction, heat and mass transfer enhance (or aid) each other. This kind of flows are called "aiding flows". Similarly, if heat and mass transfer occur in the reverse direction, heat and mass transfer hinder (or oppose) each other. This kind of flows are called "opposing flows".

In this thesis, aiding and opposing flows are investigated by simulating 3 cases. In the case I, a pure natural convection problem is simulated for $Ra_T = 2 \times 10^4$ and $Ra_S = 0$. In the case II, aiding double diffusion is simulated for $Ra_T = 10^4$, $Ra_S = 10^4$ and $Le = 1$. In the case III, opposing double diffusion is simulated for $Ra_T = 10^4$,

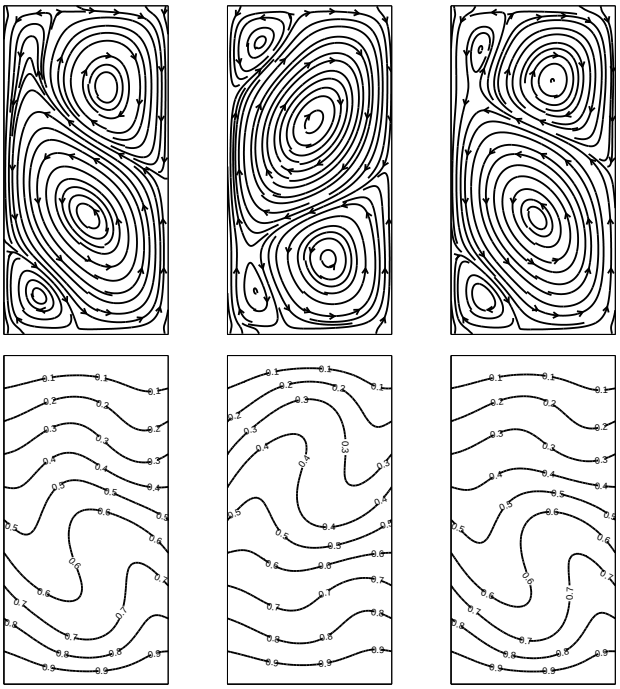

(a) 11330 (b) 14650 (c) 15800

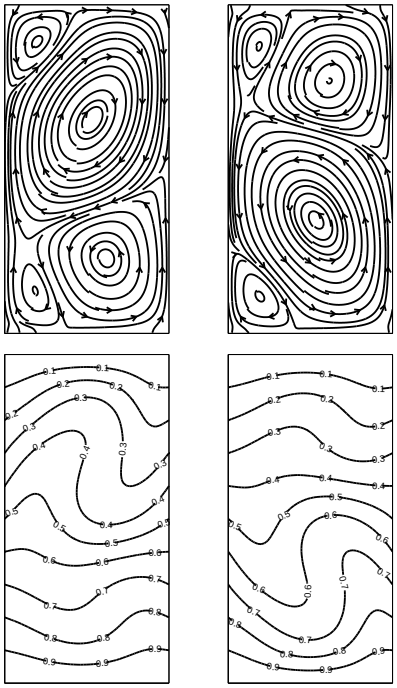

(d) 16900 (e) 18040

Figure 4.15. Streamlines and Temperatures at Different Time Steps.

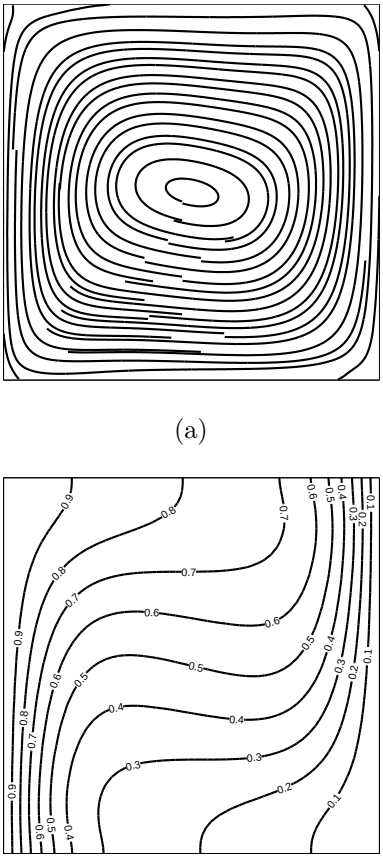

(a)

(b)

Figure 4.16. (a)Streamlines (b)Isotherms for Pure Natural Convection at $Ra_T = 2 \times 10^4$ and $Ra_S = 0$.

$Ra_S = -10^4$ and $Le = 1$.

In Figure 4.16 and 4.17, results for the cases I and II are depicted respectively. Since there is an aiding flow in case II, streamlines and isotherms are the same for both cases I and II. In addition, in case II, temperature and concentration are identical because Lewis number is set as $Le = 1$.

Moreover, in case III, all particles are stationary since heat transfer and mass transfer have an equal but opposite influence on the flow field. As a result, linear isotherms and iso-concentrations are obtained as depicted in Figure 4.18. Therefore, the ISPH code is validated for double diffusion simulations and is able to solve different type of double diffusion problems.

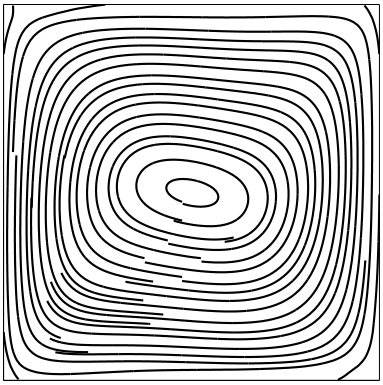

(a)

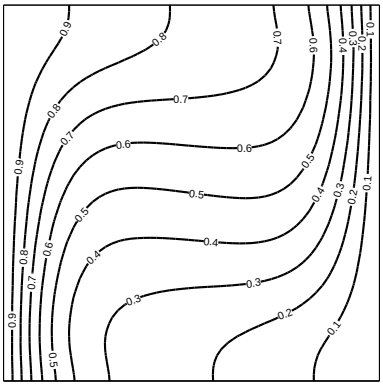

(b)

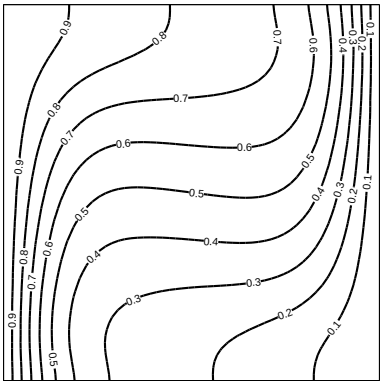

(c)

Figure 4.17. (a)Streamlines (b)Isotherms (c)Isoconcentrations for Aiding Double Diffusion at $Ra_T = 10^4$, $Ra_S = 10^4$ and $Le = 1$.

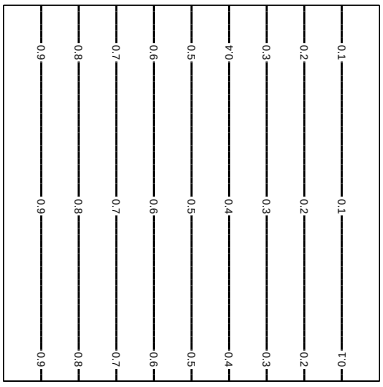

(a)

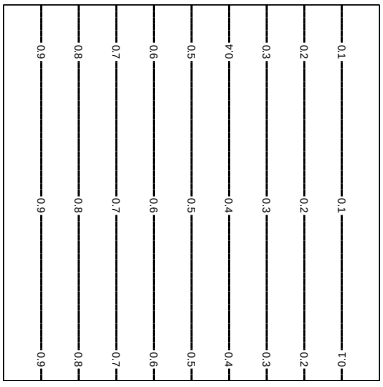

(b)

Figure 4.18. (a)Isotherms (b)Isoconcentrations for Opposing Double Diffusion at $Ra_T = 10^4$, $Ra_S = -10^4$ and $Le = 1$.

4.5. Two-phase Flow

In this thesis, ISPH code is also implemented to simulate two-phase flows. Topological changes of interfaces (e.g. rising bubble, droplet fall, bursting bubble and droplet fall on a free surface) and Rayleigh-Taylor instability are studied. Moreover, ISPH results of two-phase flow simulations are compared to the results obtained by Level Set method in terms of handling difficulties that arise in the during the simulations of problems with high Reynolds number, high density and viscosity ratio, splashing of a droplet on a solid surface and topological changes like merging and pinching off.

In order to make a better comparison of these methods, certain adjustments are made. Firstly, half of the interface thickness in LS is set $\varepsilon = 4dx$ as depicted in Figure 4.19. This is approximately equal to radius of neighborhood of a particle in SPH, $3h \approx 4dx$. Therefore, density and viscosity are smoothed in a region across the interface that has approximately same thickness in both methods. Another adjustment made is that surface tension is not considered in the simulations. This is because surface tension is modeled differently in LS and SPH.

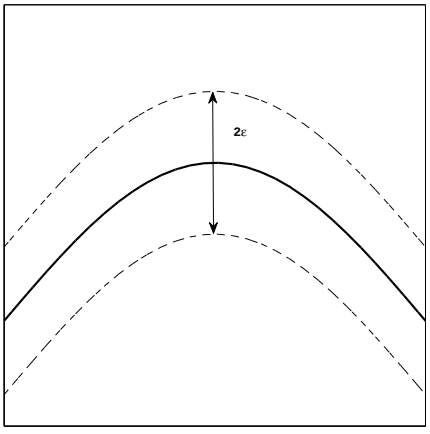

Figure 4.19. Interface thickness in Level Set simulations.

For LS simulations, 60×60 grids are used while for SPH simulation, 3600 particles are used. The geometry is a square cavity of dimensionless length 1 for all test cases.

Reynolds number is defined as $Re = \rho_1 U_c L/\mu_1$ where characteristic velocity, U_c, is defined as $U_c = \sqrt{gL}$, ρ_1 and μ_1 correspond to density and viscosity of heavier fluid respectively. Results are depicted in dimensionless time step for each test case where $\bar{t} = \sqrt{L/g}$ is the characteristic time scale. Moreover, in ISPH simulation, particle shifting method due to Xu [13] is implemented.

4.5.1. Topological Changes of Interfaces

In the first test case is the rising of a gas bubble in a surrounding liquid. This is a very important and well known problem of multiphase flows for those dealing with bubbly flows. In this case, an extremely large density ratio , $\rho_1/\rho_2 = 1000$, a large viscosity ratio, $\mu_1/\mu_2 = 100$, and a high Reynolds number, $Re = 1000$, are considered. Initially, bubble has a radius of $R = 0.125$ and its center is located at $(x_c, y_c) = (0, -0.3)$. The Level Set function is defined $\phi = \sqrt{(x - x_c)^2 + (y - y_c)^2} - R$. The lighter gas bubble experiences shape changes while it is rising due to buoyancy forces. As it is observed in Figure 4.20, both methods show relatively good agreement at first time steps, however little differences appear later on. This may be due to lack of mass conservation in LS.

Another test case is the opposite case of rising bubble problem. It is the falling of a denser fluid droplet in the surrounding lighter fluid. Reynolds number, density and viscosity ratios are set as rising bubble case. Initially, bubble has a radius of $R = 0.125$ and its center is located at $(x_c, y_c) = (0, 0.3)$. The Level Set function is defined as $\phi = R - \sqrt{(x - x_c)^2 + (y - y_c)^2}$. It is observed that liquid droplet splashes as it hits the ground and spreads in two sides on the ground surface. Results obtained by two methods are depicted in Fig(4.21). Both methods showed satisfying performance in capturing the interface and its evolution during the simulation compared to rising bubble case.

The other case is the bursting of a gas bubble at the free surface where the bubble rises until it meets and merges with the free surface. Similarly, Reynolds number, density and viscosity rations are the same as previous cases. Initially, free surface is

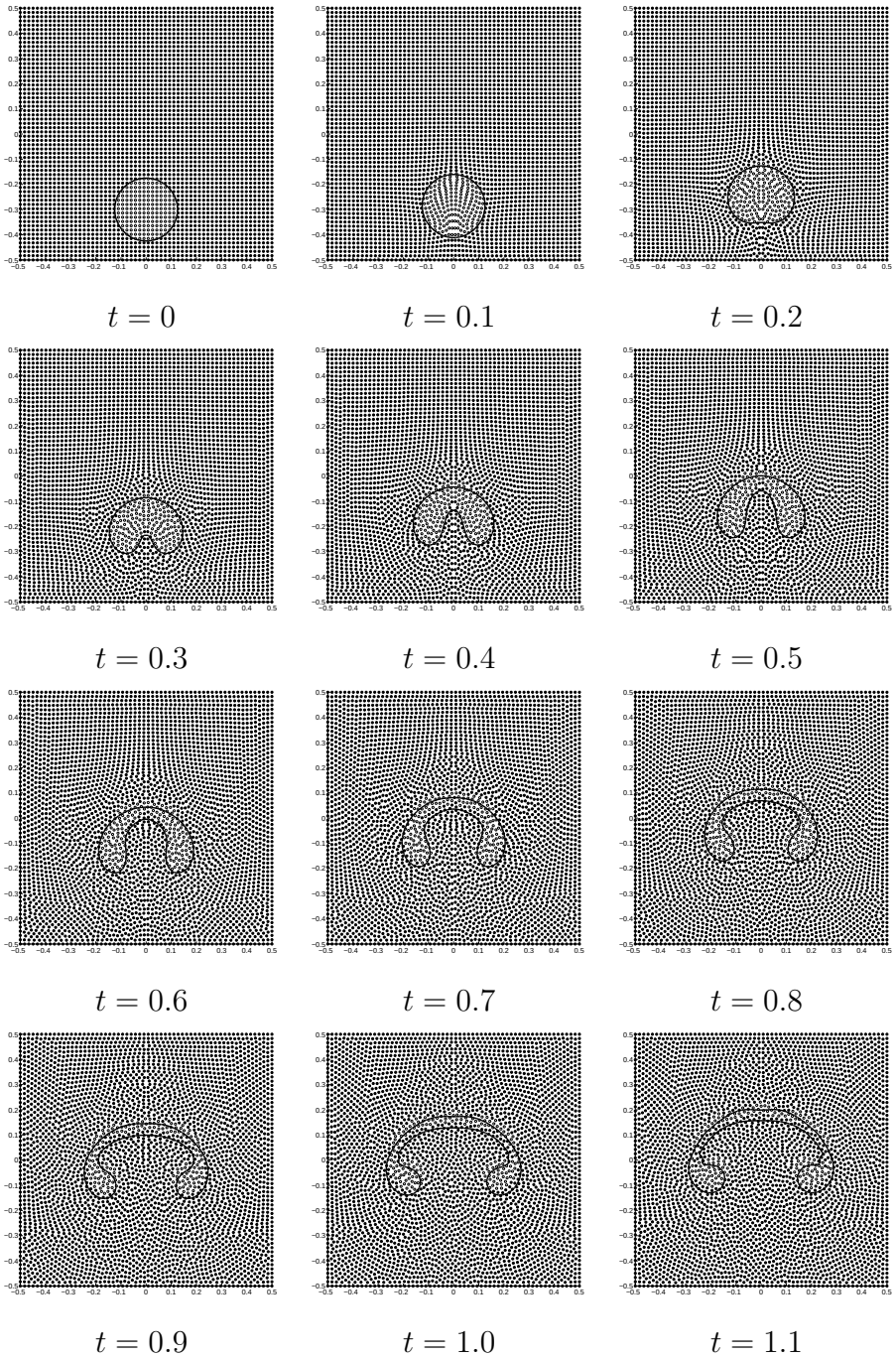

Figure 4.20. Rising Bubble: — represent Level Set Function, ● represents high density particles and ○ represents low density particles.

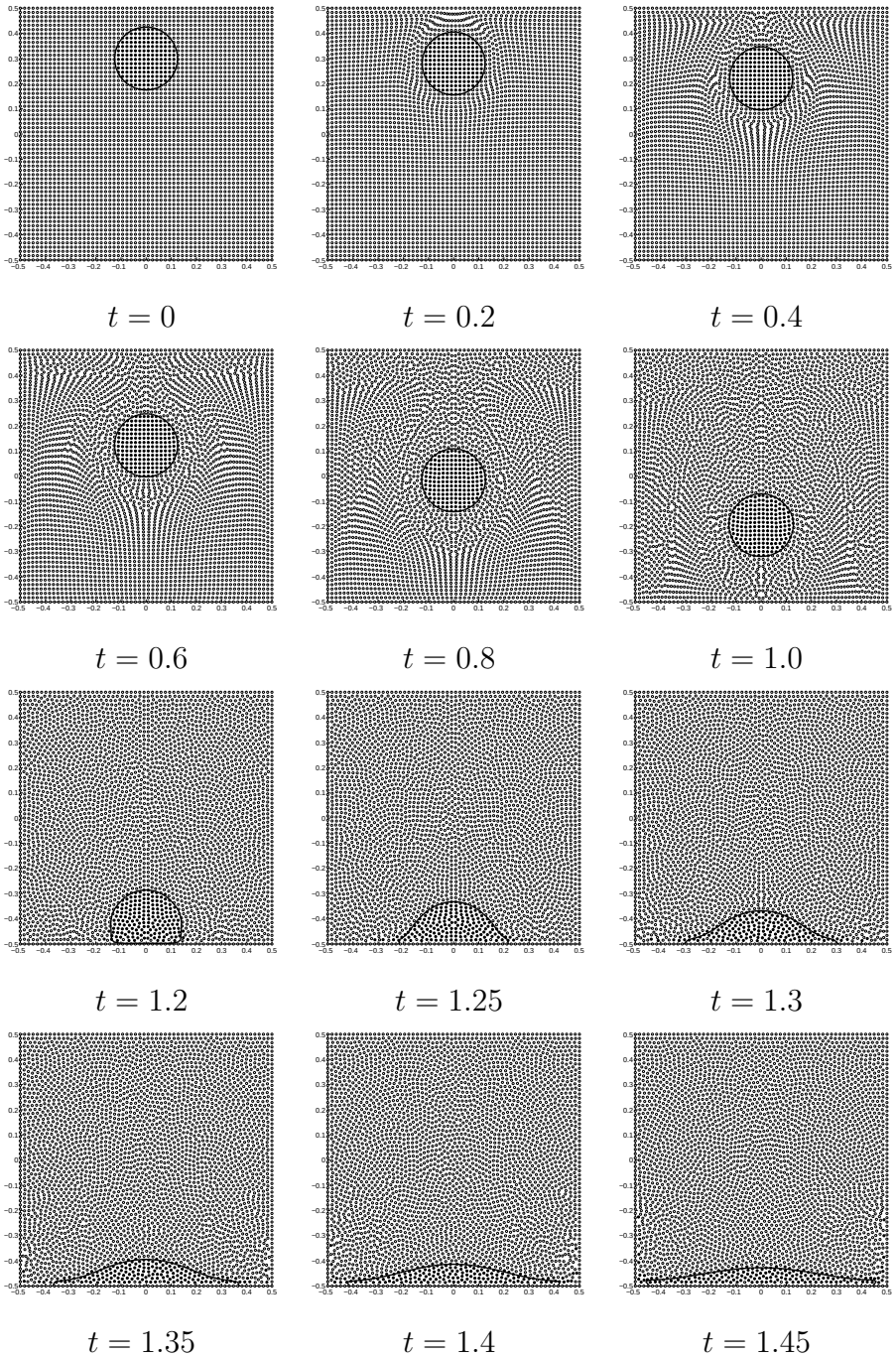

Figure 4.21. Droplet Fall: — represent Level Set Function, ● represents high density particles and ○ represents low density particles.

located at $y_s = -0.2$, bubble has a radius of $R = 0.125$ and its center is located at $(x_c, y_c) = (0, -0.35)$. The Level Set function is defined by defining two functions $\phi_1 = \sqrt{(x - x_c)^2 + (y - y_c)^2} - R$, $\phi_2 = y_s - y$ and taking the minimum of them $\phi = min(\phi_1, \phi_2)$. In Figure 4.22, it is seen that a fluid jet is formed after bubble merges with the free surface. Although both LS and SPH could capture merging and jet formation phenomena, differences are observed in LS and SPH results in terms of drop release. For instance, SPH captures fluid drops emanating from the liquid film above the bubble at the initial state and the fluid jet formed after the merging while these drops are not observed in LS results.

In last example of topological changes, droplet falls onto a free surface and merges with it. This is the opposite case of the bursting bubble problem. Reynolds number, density and viscosity rations are the same as bursting bubble case. Initially, free surface is located at $y_s = -0.2$, bubble has a radius of $R = 0.125$ and its center is located at $(x_c, y_c) = (0, -0.05)$. The Level Set function is defined by defining two functions $\phi_1 = R - \sqrt{(x - x_c)^2 + (y - y_c)^2}$, $\phi_2 = y - y_s$ and taking the maximum of them $\phi = max(\phi_1, \phi_2)$. In Figure 4.23, good agreement between the results obtained by LS and SPH is observed. However, SPH captures that gas bubbles just below the liquid droplet at the initial state are trapped and dispersed in liquid as droplet merges with free surface.

4.5.2. Rayleigh-Taylor Instability

Rayleigh-Taylor instability is considered in order to show the ability of LS and SPH methods in capturing evolution of interface. A square domain is filled by two fluids with different densities while the heavier one placed on the top of the lighter one. Density and viscosity ratios are chosen to be $\rho_1/\rho_2 = 2$ and $\mu_1/\mu_2 = 1$ respectively, and the Reynolds number is set to be $Re = 400$. The initial perturbation is imposed by defining the sinusoidal function like $Y = Asin(\omega x) - Y_0$ at the interface where A is the amplitude and ω is the frequency of this perturbation. In this case, $A = 0.15$, $\omega = 2\pi$, and $Y_0 = 0.5$. As depicted in Figure 4.24, great agreement between LS and SPH simulation of interface evolution at different times is achieved.

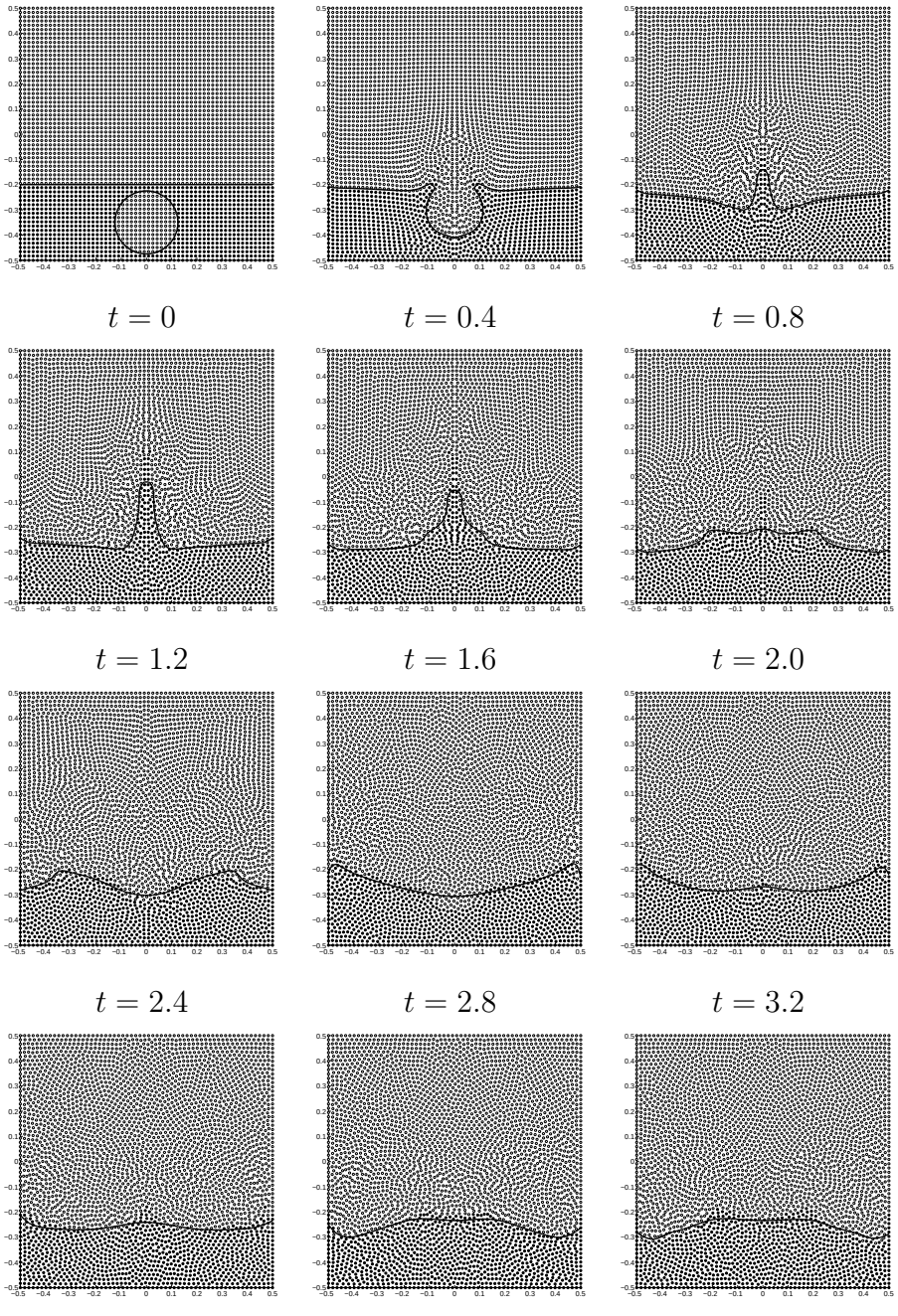

$t = 0$ $t = 0.4$ $t = 0.8$

$t = 1.2$ $t = 1.6$ $t = 2.0$

$t = 2.4$ $t = 2.8$ $t = 3.2$

$t = 3.6$ $t = 4.0$ $t = 4.4$

Figure 4.22. Bursting Bubble: — represent Level Set Function, ● represents high density particles and ○ represents low density particles.

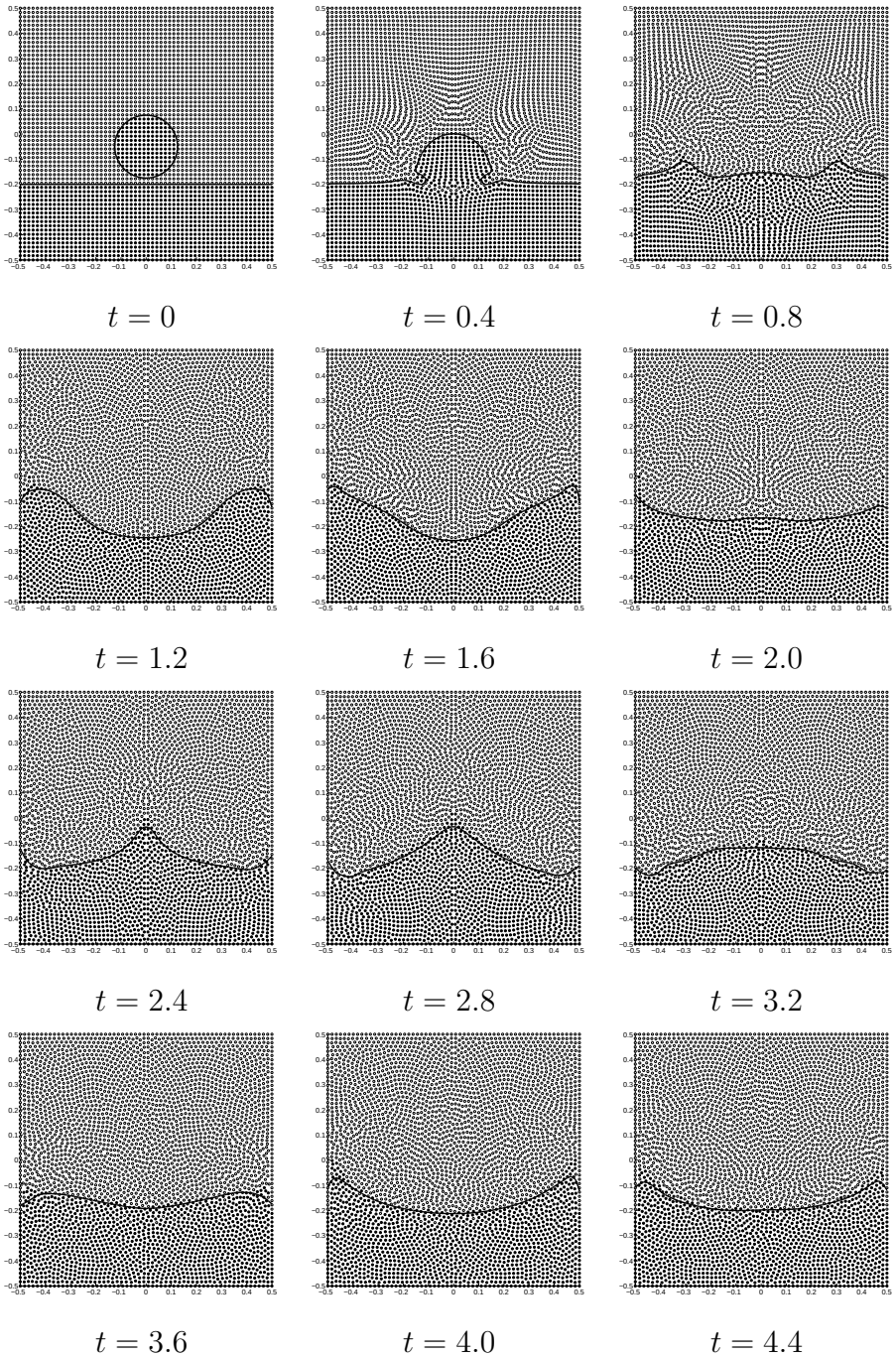

Figure 4.23. Droplet Fall onto a Free Surface: — represent Level Set Function, ● represents high density particles and ○ represents low density particles.

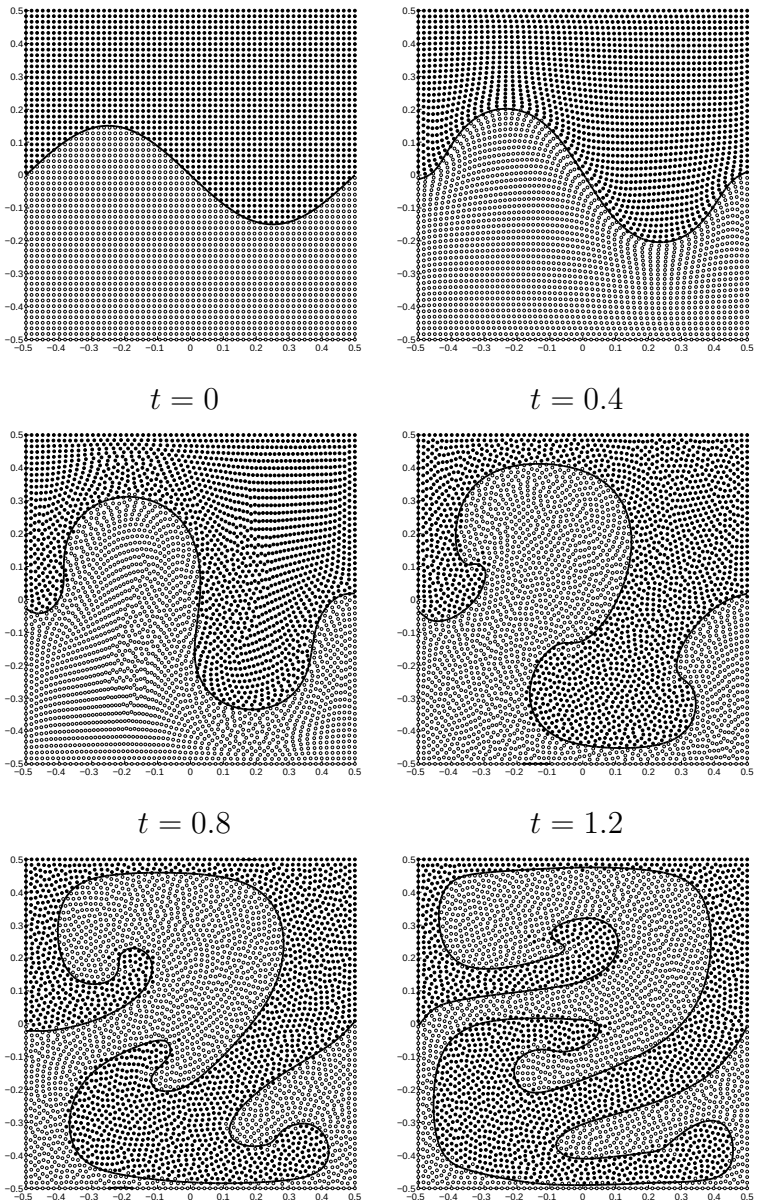

$t = 0$ $t = 0.4$

$t = 0.8$ $t = 1.2$

$t = 1.6$ $t = 2$

Figure 4.24. Rayleigh-Taylor Instability: — represent Level Set Function, ● represents high density particles and ○ represents low density particles.

5. CONCLUSIONS

In this study, convective-diffusive transport is investigated using the Incompressible Smoothed Particle Hydrodynamics (ISPH) technique. ISPH code developed during the thesis study is validated for isothermal problems such as lid-driven cavity and vortex spin-down problem. In lid-driven cavity problem, flow field is simulated at Reynolds numbers $Re = 100$, $Re = 400$ and $Re = 1000$ while in vortex spin-down problem, flow is simulated at $Re = 10$, $Re = 100$ and $Re = 1000$. Results obtained for both problems are compared to ISPH results obtained in [13] and a very good agreement is achieved.

Moreover, a grid-based ISPH approach is proposed in order to examine the upper limit accuracy of ISPH computations and this approach is implemented to natural convection in a square cavity problem. For this problem, effect of Rayleigh number is investigated in the range of $Ra = 10^3 - 10^6$. Results are compared to the data available in the literature and it is seen that grid-based ISPH results are very close to the results presented in [36–39]. In addition to grid-based ISPH code, a meshless ISPH code is employed in natural convection problems. Using the meshless ISPH code, Rayleigh-Bénard convection is simulated. A constant Rayleigh number of $Ra = 15000$ is set and different initial conditions on velocity are considered. It is seen that ISPH is code is able to obtain multiple states of solutions. It is worth nothing that multiplicity in the solutions is dependent on initial conditions. In fact, if all particles are stationary at the beginning of a simulation for a problem where boundary and initial conditions for temperature are symmetric with respect to the vertical axis in the middle of the cavity, a physical solution will not be obtained. Thus, initial velocity field can be thought as an initial disturbance that favors one of the multiple solutions. Furthermore, effect of aspect ratio on natural convection is investigated. For a constant Rayleigh number of $Ra = 15000$ is set and aspect ratios $AR = 1$ $AR = 1.5$ and $AR = 2$ are considered. It is seen that flow is stable and a steady state can be reached for $AR = 1$. On the other hand, a periodic steady state is obtained for $AR = 1.5$ and $AR = 2$ where multicellular structures and temperature profile oscillate. Consequently, heat transfer

is affected and it also shows an oscillation.

Similar to natural convection, ISPH technique is introduced to double-diffusive transport problems by proposing an appropriate projection scheme. ISPH code is used to solve aiding and opposing flow problems. In aiding flows, solutal and thermal gradients influence the flow in the same direction. In opposing flows, solutal and thermal gradients are in the opposite directions. If the effect of solutal gradients are eliminated, in other words, if solutal Rayleigh number is set to be zero, $Ra_S = 0$, double-diffusion problem becomes a pure natural convection problem. For this reason, a pure natural convection problem is considered where $Ra_T = 20000$ and $Ra_S = 0$. Then, an aiding double-diffusive flow is considered where $Ra_T = 10000$, $Ra_S = 10000$ and $Le = 1$. Since Lewis number, Le, is equal to unity, solutions of temperature and concentration fields are equal to each other and they also equal to the temperature field obtain in pure natural convection problem at $Ra_T = 20000$. Likewise, an opposing flow is considered where $Ra_T = 10000$, $Ra_S = -10000$ and $Le = 1$. For this case, it is seen that particles remain stationary and a linear temperature and concentration field is obtained. These two tests validates accuracy of ISPH code in double-diffusive transport.

Apart from the single-phase flow, ISPH code is implemented to two-phase flows. In this case, topological changes of interfaces and Rayleigh-Taylor instability problem are considered. The ISPH results are compared to results obtained by using Level Set method. In terms of topological changes of interfaces, rising bubble, droplet fall, bursting bubble at the free surface and droplet fall on the free surface problems are simulated. For each case, a heavier fluid of density $\rho_1 = 1000$ and a lighter fluid of density $\rho_2 = 1$ are considered and Reynolds number is set to be $Re = 1000$. It is seen that ISPH and Level Set results are in a good agreement when the continuous phase is consist of lighter fluid ad the results show observable differences when the continuous phase is consist of the heavier fluid. This may be due to the fact that mass is exactly conserved in ISPH simulations and not conserved in Level Set simulations. Furthermore, ISPH is able to capture drop release in bursting bubble at the free surface and droplet fall onto the free surface problems.

REFERENCES

1. Lucy, L., "A numerical approach to the testing of the fission hypothesis", *The Astronomical Journal*, Vol. 82, pp. 1013–1024, 1977.

2. Gingold, R. and J. Monaghan, "Smoothed particle hydrodynamics-theory and application to non-spherical stars", *Monthly Notices of the Royal Astronomical Society*, Vol. 181, pp. 375–389, 1977.

3. Liu, G. and M. Liu, *Smoothed particle hydrodynamics: a meshfree particle method*, World Scientific Pub Co Inc, 2003.

4. Monaghan, J., "Simulating free surface flows with SPH", *Journal of Computational Physics*, Vol. 110, No. 2, pp. 399–406, 1994.

5. Morris, J., P. Fox and Y. Zhu, "Modeling low Reynolds number incompressible flows using SPH", *Journal of Computational Physics*, Vol. 136, No. 1, pp. 214–226, 1997.

6. Gomez-Gesteira, M., B. Rogers, A. Crespo, R. Dalrymple, M. Narayanaswamy and J. Dominguez, "SPHysics-development of a free-surface fluid solver-part 1: theory and formulations", *Computers & Geosciences*, Vol. 48, pp. 289–299, 2012.

7. Shao, J., H. Li, G. Liu and M. Liu, "An improved SPH method for modeling liquid sloshing dynamics", *Computers & Structures*, Vol. 100, pp. 18–26, 2012.

8. Cummins, S. and M. Rudman, "An SPH projection method", *Journal of Computational Physics*, Vol. 152, No. 2, pp. 584–607, 1999.

9. Shao, S. and E. Lo, "Incompressible SPH method for simulating Newtonian and non-Newtonian flows with a free surface", *Advances in Water Resources*, Vol. 26, No. 7, pp. 787–800, 2003.

10. Pozorski, J. and A. Wawrenczuk, "SPH computation of incompressible viscous flows", *Journal of Theoretical and Applied Mechnanics*, Vol. 40, pp. 917–937, 2002.

11. Colin, F., R. Egli and F. Lin, "Computing a null divergence velocity field using smoothed particle hydrodynamics", *Journal of Computational Physics*, Vol. 217, No. 2, pp. 680–692, 2006.

12. Hu, X. and N. Adams, "An incompressible multi-phase SPH method", *Journal of Computational Physics*, Vol. 227, No. 1, pp. 264–278, 2007.

13. Xu, R., P. Stansby and D. Laurence, "Accuracy and stability in incompressible SPH (ISPH) based on the projection method and a new approach", *Journal of Computational Physics*, Vol. 228, No. 18, pp. 6703–6725, 2009.

14. Szewc, K., J. Pozorski and J. Minier, "Analysis of the incompressibility constraint in the Smoothed Particle Hydrodynamics method", *International Journal for Numerical Methods in Engineering*, Vol. 92, No. 4, pp. 343–369, 2012.

15. Hosseini, S., M. Manzari and S. Hannani, "A fully explicit three-step SPH algorithm for simulation of non-Newtonian fluid flow", *International Journal of Numerical Methods for Heat & Fluid Flow*, Vol. 17, No. 7, pp. 715–735, 2007.

16. van der Vorst, H. A., "BI-CGSTAB: a fast and smoothly converging variant of BI-CG for the solution of nonsymmetric linear systems", *SIAM Journal on Scientific and Statistical Computing*, Vol. 13, No. 2, pp. 631–644, 1992.

17. Ellero, M., M. Serrano and P. Espanol, "Incompressible smoothed particle hydrodynamics", *Journal of Computational Physics*, Vol. 226, No. 2, pp. 1731–1752, 2007.

18. Chaniotis, A., D. Poulikakos and P. Koumoutsakos, "Remeshed smoothed particle hydrodynamics for the simulation of viscous and heat conducting flows", *Journal of Computational Physics*, Vol. 182, No. 1, pp. 67–90, 2002.

19. Szewc, K., J. Pozorski and A. Tanière, "Modeling of natural convection with Smoothed Particle Hydrodynamics: Non-Boussinesq formulation", *International Journal of Heat and Mass Transfer*, Vol. 54, No. 23–24, pp. 4807–4816, 2011.

20. Monaghan, J., "SPH without a tensile instability", *Journal of Computational Physics*, Vol. 159, No. 2, pp. 290–311, 2000.

21. Roache, P., "Quantification of uncertainty in computational fluid dynamic", *Annual Review of Fluid Mechanics*, Vol. 29, pp. 123–160, 1997.

22. Oden, J. and K. Vemaganti, "Estimation of local modeling error and goal-oriented adaptive modeling of heterogeneous materials I. Error estimates and adaptive algorithms", *Journal of Computational Physics*, Vol. 164, No. 1, pp. 22–47, 2000.

23. Afshar, M. and G. Shobeyri, "Efficient simulation of free surface flows with discrete least-squares meshless method using a priori error estimator", *International Journal of Computational Fluid Dynamics*, Vol. 24, No. 9, pp. 349–367, 2010.

24. Prudhomme, S. and J. Oden, "Computable error estimators and adaptive techniques for fluid flow problems", *Lecture Notes in Computational Science and Engineering*, Vol. 25, pp. 207–268, 2002.

25. Prudhomme, S. and J. Oden, "A posteriori error estimation and error control for finite element approximations of the time-dependent Navier–Stokes equations", *Finite Elements in Analysis and Design*, Vol. 33, No. 4, pp. 247–262, 1999.

26. Ciarlet, P., *The finite element method for elliptic problems*, Vol. 4, North Holland, 1978.

27. Ren, J., J. Ouyang, B. Yang, T. Jiang and H. Mai, "Simulation of container filling process with two inlets by improved smoothed particle hydrodynamics (SPH) method", *International Journal of Computational Fluid Dynamics*, Vol. 25, No. 7, pp. 365–386, 2011.

28. Schoenberg, I., "Contributions to the problem of approximation of equidistant data by analytic functions", *Quart. Appl. Math*, Vol. 4, No. Part A, pp. 45–99, 1946.

29. Dehnen, W. and H. Aly, "Improving convergence in smoothed particle hydrodynamics simulations without pairing instability", *Monthly Notices of the Royal Astronomical Society*, Vol. 425, No. 2, pp. 1068–1082, 2012.

30. Cleary, P. and J. Monaghan, "Conduction modelling using smoothed particle hydrodynamics", *Journal of Computational Physics*, Vol. 148, No. 1, pp. 227–264, 1999.

31. Dilts, G., "Moving-least-squares particle hydrodynamics–I. consistency and stability", *International Journal for Numerical Methods in Engineering*, Vol. 44, No. 8, pp. 1115–1155, 1999.

32. Randles, P. and L. Libersky, "Smoothed particle hydrodynamics: some recent improvements and applications", *Computer Methods in Applied Mechanics and Engineering*, Vol. 139, No. 1, pp. 375–408, 1996.

33. Chen, J. and J. Beraun, "A generalized smoothed particle hydrodynamics method for nonlinear dynamic problems", *Computer Methods in Applied Mechanics and Engineering*, Vol. 190, No. 1, pp. 225–239, 2000.

34. Oger, G., M. Doring, B. Alessandrini and P. Ferrant, "An improved SPH method: Towards higher order convergence", *Journal of Computational Physics*, Vol. 225, No. 2, pp. 1472–1492, 2007.

35. Liu, M. and G. Liu, "Smoothed particle hydrodynamics (SPH): an overview and recent developments", *Archives of Computational Methods in Engineering*, Vol. 17, No. 1, pp. 25–76, 2010.

36. de Vahl Davis, G., "Natural convection of air in a square cavity: a bench mark numerical solution", *International Journal for Numerical Methods in Fluids*, Vol. 3,

No. 3, pp. 249–264, 1983.

37. Barakos, G., E. Mitsoulis and D. Assimacopoulos, "Natural convection flow in a square cavity revisited: laminar and turbulent models with wall functions", *International Journal for Numerical Methods in Fluids*, Vol. 18, No. 7, pp. 695–719, 1994.

38. Wakashima, S. and T. Saitoh, "Benchmark solutions for natural convection in a cubic cavity using the high-order time–space method", *International Journal of Heat and Mass Transfer*, Vol. 47, No. 4, pp. 853–864, 2004.

39. Fusegi, T., J. Hyun and K. Kuwahara, "Three-dimensional simulations of natural convection in a sidewall-heated cube", *International Journal for Numerical Methods in Fluids*, Vol. 13, No. 7, pp. 857–867, 1991.